

1 SEARCH FOR  $t\bar{t}Z' \rightarrow t\bar{t}t\bar{t}$  PRODUCTION IN THE MULTILEPTON FINAL STATE IN  
2  $pp$  COLLISIONS AT  $\sqrt{s} = 13$  TEV WITH THE ATLAS DETECTOR

3 By

4 Hieu Le

5 A DISSERTATION

6 Submitted to  
7 Michigan State University  
8 in partial fulfillment of the requirements  
9 for the degree of

10 Physics — Doctor of Philosophy

11 2025

**ABSTRACT**

13 Lorem ipsum dolor sit amet, consectetur adipiscing elit, sed do eiusmod tempor incididunt ut  
14 labore et dolore magna aliqua. Ut enim ad minim veniam, quis nostrud exercitation ullamco  
15 laboris nisi ut aliquip ex ea commodo consequat. Duis aute irure dolor in reprehenderit in  
16 voluptate velit esse cillum dolore eu fugiat nulla pariatur. Excepteur sint occaecat cupidatat  
17 non proident, sunt in culpa qui officia deserunt mollit anim id est laborum.

**ACKNOWLEDGMENTS**

- 19 Advisor: Reinhard Schwienhorst
- 20 Postdoc: Binbin Dong
- 21 Committee
- 22 MSU group
- 23 ATLAS analysis group
- 24 Friend: Daniel, Grayson, Bella, Eric, Jordan
- 25 Other friends: Jasper, Adam, Brittany
- 26 Parents
- 27 Spouse: Allen Sechrist
- 28 ATLAS in general & funding agencies

**PREFACE**

30 This is my preface. remarks remarks remarks

# TABLE OF CONTENTS

31	<b>List of Tables</b>	<b>vii</b>
32	<b>List of Figures</b>	<b>viii</b>
33	<b>KEY TO ABBREVIATIONS</b>	<b>ix</b>
34	<b>Roadmap</b>	<b>1</b>
35	<b>Chapter 1. Introduction</b>	<b>2</b>
36	<b>Chapter 2. Theoretical Overview</b>	<b>3</b>
37	2.1 The Standard Model	3
38	2.1.1 Elementary particles	3
39	2.1.2 Mathematical formalism	7
40	2.1.2.1 Quantum chromodynamics	8
41	2.1.2.2 Electroweak theory	10
42	2.1.2.3 Higgs mechanism	13
43	2.2 Beyond the Standard Model	16
44	2.2.1 Top-philic vector resonance	16
45	2.2.2 BSM four-top quark production	19
46	<b>Chapter 3. LHC &amp; ATLAS Experiment</b>	<b>21</b>
47	3.1 The Large Hadron Collider	21
48	3.1.1 Overview	21
49	3.1.2 LHC operations	21
50	3.2 The ATLAS detector	22
51	3.2.1 Inner detector	24
52	3.2.2 Calorimeter systems	25
53	3.2.3 Muon spectrometer	27
54	3.2.4 Forward detectors	29
55	3.2.5 Magnetic systems	29
56	3.2.6 Trigger & data acquisition	29
57	<b>Chapter 4. Particle Reconstruction &amp; Identification</b>	<b>31</b>
58	4.1 Primary reconstruction	31
59	4.1.1 Tracks	31
60	4.1.2 Vertices	32
61	4.1.3 Topological clusters	33
62	4.2 Jets	35
63	4.2.1 Jet reconstruction	35
64	4.2.2 Flavor tagging	36
65	4.3 Leptons	40

66	4.3.1	Electrons . . . . .	40
67	4.3.2	Muons . . . . .	43
68	4.4	Missing transverse momentum . . . . .	45
69	4.5	Overlap removal . . . . .	46
70	4.6	Object definition . . . . .	47
71	<b>Chapter 5. Data &amp; Simulated Samples . . . . .</b>		<b>48</b>
72	5.1	Data samples . . . . .	48
73	5.2	Monte Carlo samples . . . . .	49
74	5.2.1	$t\bar{t}Z'$ signal samples . . . . .	49
75	5.2.2	Background samples . . . . .	51
76	<b>Chapter 6. Analysis Strategy . . . . .</b>		<b>53</b>
77	6.1	Event selection . . . . .	53
78	6.2	Analysis regions . . . . .	55
79	6.2.1	Signal regions . . . . .	55
80	6.2.2	Control regions . . . . .	56
81	6.2.3	Validation regions . . . . .	58
82	6.3	Background estimation . . . . .	58
83	6.3.1	Template fitting for fake/non-prompt estimation . . . . .	60
84	6.3.2	Charge misidentification data-driven estimation . . . . .	61
85	6.3.3	$t\bar{t}W$ background data-driven estimation . . . . .	63
86	<b>Chapter 7. Systematic Uncertainties . . . . .</b>		<b>67</b>
87	7.1	Experimental uncertainties . . . . .	67
88	7.1.1	Leptons . . . . .	67
89	7.1.2	Jets . . . . .	68
90	7.1.3	Missing transverse energy . . . . .	70
91	7.2	Modeling uncertainties . . . . .	70
92	7.2.1	Signal and irreducible background uncertainties . . . . .	70
93	7.2.2	Reducible background uncertainties . . . . .	73
94	<b>Chapter 8. Results . . . . .</b>		<b>76</b>
95	8.1	Statistical analysis . . . . .	76
96	8.1.1	Profile likelihood fit . . . . .	76
97	8.1.2	Exclusion limits . . . . .	78
98	8.2	Fit results . . . . .	78
99	<b>Chapter 9. Summary . . . . .</b>		<b>79</b>
100	<b>References . . . . .</b>		<b>80</b>

# List of Tables

102	Table 4.1: Overlap removal process for this analysis, applied sequentially from top to	
103	bottom. . . . .	47
104	Table 4.2: Summary of object selection criteria used in this analysis . . . . .	47
105	Table 5.1: Caption . . . . .	48
106	Table 5.2: Summary of all Monte-Carlo samples used in this analysis. . . . .	50
107	Table 6.1: Caption . . . . .	56
108	Table 6.2: Caption . . . . .	57
109	Table 6.3: Caption . . . . .	59
110	Table 7.1: Summary of the experimental systematic uncertainties considered in this	
111	analysis. . . . .	71
112	Table 7.2: Caption . . . . .	74
113	Table 7.3: Caption . . . . .	75

# List of Figures

114		
115	Figure 2.1: Caption . . . . .	4
116	Figure 2.2: Caption . . . . .	7
117	Figure 2.3: Caption . . . . .	19
118	Figure 2.4: Caption . . . . .	20
119	Figure 3.1: Caption . . . . .	23
120	Figure 3.2: Caption . . . . .	26
121	Figure 4.1: Stages of topo-cluster formation corresponding to each threshold. In (a),	
122	proto-clusters are seeded from cells with adequate signal significance $\zeta_{\text{cell}}^{\text{EM}}$ .	
123	The clusters are further merged and split in (b) according to a predefined	
124	cluster growth threshold. The process stops in (c) when all sufficiently	
125	significant signal hits have been matched to a cluster. . . . .	34
126	Figure 4.2: Jet energy scale calibration sequence for EM-scale jets. . . . .	36
127	Figure 4.3: Overview of the GN2 architecture. The number of jet and track features	
128	are represented by $n_{\text{jf}}$ and $n_{\text{tf}}$ respectively. The global jet representation	
129	and track embeddings output by the Transformer encoder are used as	
130	inputs for three task-specific networks. . . . .	38
131	Figure 4.4: The $c$ -, light- and $\tau$ -jet rejection rate as a function of $b$ -tagging efficiency	
132	for GN2 and DL1d using (a) jets in the $t\bar{t}$ sample, and (b) jets in the $Z'$	
133	sample. The performance ratios of GN2 to DL1d are shown in the bottom	
134	panels. . . . .	39



## KEY TO ABBREVIATIONS

### Physical & mathematical quantities

$\chi^2$  chi-squared

$\Delta R$  angular distance

$\eta$  pseudorapidity

$E_T$  transverse energy

$E_T^{\text{miss}}$  missing transverse momentum

$\gamma_\mu$  Dirac matrices

$I$  weak isospin

$L$  instantaneous luminosity

$\mu$  signal strength

$p_T$  transverse momentum

### Particles

$b$  bottom quark

$pp$  proton-proton

$t\bar{t}$  top/anti-top quark

$t\bar{t}t\bar{t}$  four-top-quark

$tW$  single-top

### Acronyms

**1LOS** one lepton, or two leptons of opposite charges

**AF3** AtlFast3 fast simulation

**ATLAS** A Toroidal LHC ApparatuS

**BDT** boosted decision tree

**BSM** Beyond the Standard Model

**CERN** European Organization for Nuclear Research

160 **CKM** CabibboKobayashiMaskawa matrix  
161 **CMS** Compact Muon Solenoid  
162 **CR** control region  
163 **CSC** Cathode Strip Chambers  
164 **ECIDS** Electron Charge ID Selector  
165 **EM** electromagnetic  
166 **EW** electroweak  
167 **FS** full detector simulation  
168 **GNN** graph neural network  
169 **GSF** Gaussian-sum filter  
170 **GUT** Grand Unified Theory  
171 **HLT** High-Level Trigger  
172 **ID** inner detector  
173 **JER** jet energy resolution  
174 **JES** jet energy scale  
175 **JVT** Jet Vertex Tagger  
176 **L1** Level 1  
177 **LH** likelihood  
178 **LLH** log-likelihood  
179 **LO** leading order  
180 **LAr** liquid argon  
181 **LHC** Large Hadron Collider  
182 **MC** Monte Carlo simulation  
183 **ME** matrix element  
184 **MS** muon spectrometer  
185 **MDT** Monitored Drift Tubes  
186 **MET** missing transverse energy

187 **NF** normalization factor  
 188 **NLO** next-to-leading order  
 189 **NNLO** next-to-next-to-leading order  
 190 **NP** nuisance parameter  
 191 **OP** operating point (also called working point)  
 192 **PCBT** pseudo-continuous  $b$ -tagging  
 193 **PDF** parton distribution function  
 194 **POI** parameter of interest  
 195 **PS** parton shower  
 196 **PV** primary vertex  
 197 **QCD** quantum chromodynamics  
 198 **QED** quantum electrodynamics  
 199 **QFT** quantum field theory  
 200 **QmisID** charge mis-identification  
 201 **SCT** Semiconductor Tracker  
 202 **SF** scale factor  
 203 **SM** Standard Model  
 204 **SR** signal region  
 205 **SSML** two leptons of the same charge, or more than two leptons (multilepton)  
 206 **TDAQ** Trigger and Data Acquisition  
 207 **TRT** Transition Radiation Tracker  
 208 **VEV** vacuum expectation value

# Roadmap

209		
210	1. Finish adding bullets for all sections .....	06/04
211	Remaining	
212	• introduction	
213	2. Fill in details .....	06/13
214	• Add missing figures	
215	• Add missing bib	
216	3. Finalize analysis	
217	4. String everything together	
218	5. Miscellaneous/logistics (proofreading, review, ATLAS approval, etc.) .....	
219	6. Submission to the graduate school .....	07/01
220	7. Defense .....	07/15

# Chapter 1. Introduction

[1]

1. background and context

2. problem to be solved in thesis

3. aim of analysis:  $Z'$  consequences of many BSM theories, searching for  $Z'$

4. hypothesis/research question: searching for  $Z'$  in  $t\bar{t}t\bar{t}$  SSML channel

5. methodology: data collection -  $\sqrt{s}$  analysis regions -  $\sqrt{s}$  binned likelihood fit

6. thesis structure:

- ch2: SM/BSM theoretical background

- ch3: LHC/ATLAS experiment

- ch4: samples used in the analysis

- ch5: ATLAS particle reconstruction and identification techniques, and object definitions for the analysis

- ch6: analysis strategy

- ch7: systematic uncertainties affecting the analysis

- ch8: final results

- ch9: summary

## Chapter 2. Theoretical Overview

### 2.1 The Standard Model

The Standard Model of Physics (SM) is currently the most successful formalism to describe the physical world at a microscopic scale.

The SM provides descriptions for all currently known elementary particles and three out of four fundamental forces with the exception of gravity.

#### 2.1.1 Elementary particles

Elementary particles in the SM can be classified into two groups: bosons, consisting of particles following Bose-Einstein statistics with integer spin and fermions, consisting of particles following Fermi-Dirac statistics with half-integer spin

Fermions are the building blocks of composite particles and consequently all known matter, and can be further split into quarks & leptons.

Bosons act as force mediators for all fundamental forces described by the SM. Bosons have two types: a scalar boson with spin 0 and vector gauge bosons with spin 1.

For each elementary particle there also exists a corresponding antiparticle with identical mass and opposite charge (electric or color).

#### Fermions

Quarks and leptons each has six flavors, grouped into three generations of doublets.

The six quark flavors consist of up ( $u$ ), down ( $d$ ), charm ( $c$ ), strange ( $s$ ), bottom ( $b$ ) and top

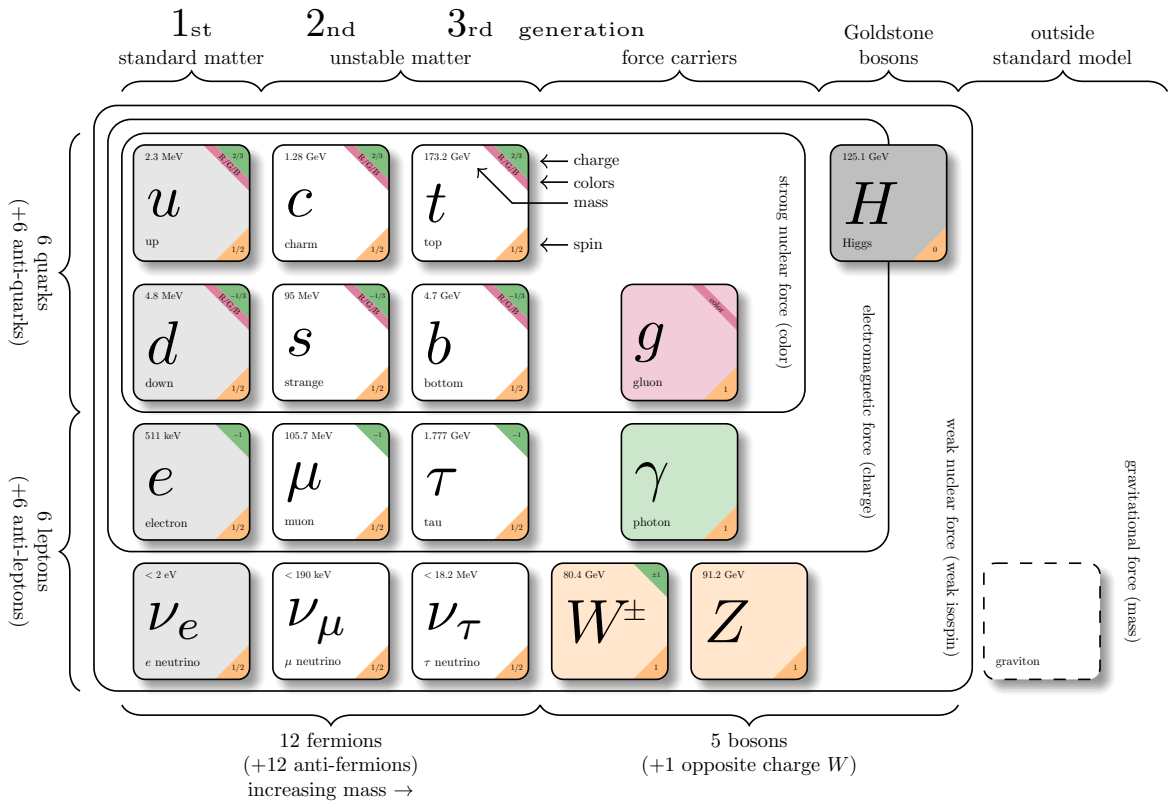


Figure 2.1: Caption[2]

( $t$ ) quark flavors in increasing order of mass, forming three doublets ( $u, d$ ), ( $c, s$ ) and ( $t, b$ ).

Each doublet consists of one quark with electric charge of  $+2/3$  ( $u, s, t$ ), and one with charge of  $-1/3$  ( $d, c, b$ ).

Each quark also has a property known as color charge, with possible values of red ( $R$ ), green ( $G$ ), blue ( $B$ ) or antired ( $\bar{R}$ ), antigreen ( $\bar{G}$ ), and antiblue ( $\bar{B}$ ). Color charge follows color confinement rules, which allows only configurations of quarks with neutral color charge to exist in isolation. Neutral charge configurations can be formed from either a set of three colors ( $R, G, B$ ), a set of a color and its anticolor ( $q, \bar{q}$ ), or any combination of the two. Consequently, no isolated quark can exist in a vacuum and can only exist in bound states called hadrons.

Quarks are the only elementary particles in the SM that can interact with all four fundamental forces.

The three leptons doublets consist of electron ( $e$ ), muon ( $\mu$ ), tau ( $\tau$ ) and their respective neutrino flavors: electron neutrino ( $\nu_e$ ), muon neutrino ( $\nu_\mu$ ) and tau neutrino ( $\nu_\tau$ )

Charged leptons ( $e, \mu, \tau$ ) carry an electric charge of  $-1$ , while their antiparticles carry the opposite charge  $+1$  and their corresponding neutrino flavors carrying no charge (charge neutral).

Charged leptons interact with all fundamental forces except the strong force, while neutrinos only interact with the weak force and gravity.

## Bosons

The SM classify bosons into two types: one scalar boson with spin 0 known as the Higgs ( $H$ ) boson, and vector gauge bosons with spin 1 known as gluons ( $g$ ), photon ( $\gamma$ ),  $W^\pm$  and  $Z$  bosons.



The gluons and photon are massless, while the  $W^\pm$ ,  $Z$  and  $H$  are massive.

Each vector gauge boson serves as the mediator for a fundamental force described by the SM.

Gluons are massless mediator particles for the strong interaction between quarks according to quantum chromodynamics (QCD), and carry the color charge in a strong interaction. Each gluon carries a non-neutral color charge out of eight linearly independent color states in the gluon color octet.

Photon is the massless and charge-neutral mediator particle for the electromagnetic interaction following quantum electrodynamics (QED).

The  $W^\pm$  and  $Z$  bosons are massive mediator particles for the weak interaction, with the  $W^\pm$  boson carrying an electric charge of  $\pm 1$  while the  $Z$  boson is charge neutral.

Other than the vector gauge boson, the only scalar boson in the SM is the Higgs boson which is massive with electric charge of 0.

The Higgs boson does not mediate a fundamental force like vector bosons, but serve to provide the rest mass for all massive elementary particles in the SM through the Higgs mechanism as described in Section 2.21refsec:higgs.

## Top quark

As of now, the top quark  $t$  is the heaviest particle in the SM with mass of about 173 GeV, compared to the heaviest fermion, the Higgs boson at 125 GeV and the second most massive fermion, the  $b$ -quark at about 4.2 GeV. This also gives it the strongest coupling to the Higgs boson and exotic resonances in various proposed BSM models (citations), making the top quark and its processes attractive vehicles with which to probe new physics.

Due to its mass, the top quark has a very short lifetime of  $10^{-24}$  s, and consequently decays

304 before it can hadronize. The top quark decays to a  $W$  boson and a  $b$ -quark with a branching  
 305 ratio of almost 100%, and is assumed to be such for the purpose of this analysis. The  $W$  boson  
 306 can subsequently decay hadronically or leptonically as shown in Figure 2.2, with branching  
 307 ratios of approximately 68% and 32% respectively and with all lepton flavors having similar  
 308 ratios assuming lepton universality.

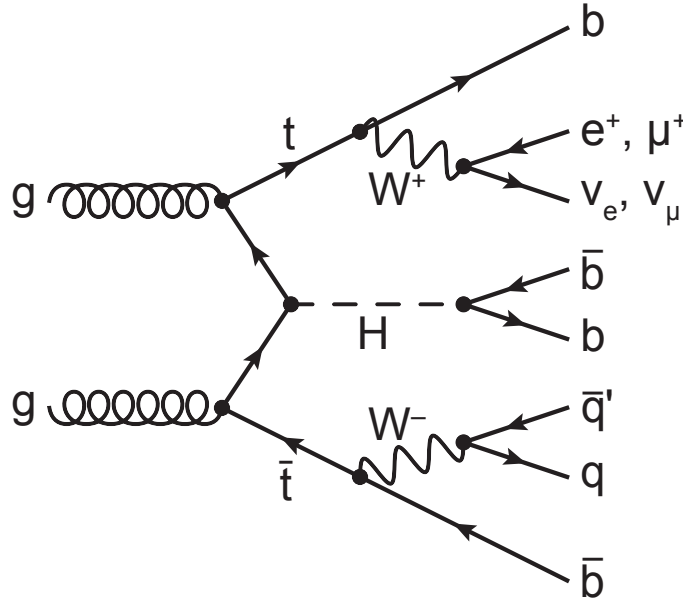


Figure 2.2:  $H \rightarrow t\bar{t}$  possible,  $t\bar{t}t\bar{t}$  final state[3]

### 309 2.1.2 Mathematical formalism

310 The SM can be described within the formalism of quantum field theory (QFT) with the  
 311 Lagrangian

$$\mathcal{L}_{\text{SM}} = \mathcal{L}_{\text{QCD}} + \underbrace{(\mathcal{L}_{\text{gauge}} + \mathcal{L}_{\text{fermion}} + \mathcal{L}_{\text{Higgs}} + \mathcal{L}_{\text{Yukawa}})}_{\mathcal{L}_{\text{EW}}} \quad (2.1)$$

312 where  $\mathcal{L}_{\text{QCD}}$  is the QCD term and  $\mathcal{L}_{\text{EW}}$  is the electroweak (EW) term of the Lagrangian.  
 313 QFT treats particles as excitations of their corresponding quantum fields: fermion field  $\psi$ ,

314 electroweak boson fields  $W_{1,2,3}$  &  $B$ , gluon field  $G_\alpha$  and Higgs field  $\phi$ .  
 315 QFT depends heavily on gauge theory. A quantum field has gauge symmetry if there exists  
 316 a continuous gauge transformation that when applied to every point (local gauge transfor-  
 317 mation) leaves the field Lagrangian unchanged. The set of gauge transformations of a gauge  
 318 symmetry is the symmetry group of the field, which comes with a set of generators, each with  
 319 a corresponding gauge field. Under QFT, the quanta of these gauge fields are called gauge  
 320 bosons. The SM Lagrangian is gauge invariant under global Poincaré symmetry and local  
 321  $SU(3)_C \times SU(2)_L \times U(1)_Y$  gauge symmetry, with the gauge term  $SU(3)_C$  corresponding to  
 322 the strong interaction and  $SU(2)_L \times U(1)_Y$  to the EW interaction.  
 323 Global Poincaré symmetry ensures that  $\mathcal{L}_{\text{SM}}$  satisfies translational symmetry, rotational  
 324 symmetry and Lorentz boost frame invariance. By Noether's theorem, gauge symmetries  
 325 lead to corresponding conservation laws which leads to conservation of momentum, angular  
 326 momentum and energy in the SM.

### 327 **2.1.2.1 Quantum chromodynamics**

328 QCD is a non-Abelian gauge theory (Yang-Mills theory) describing the strong interaction  
 329 between quarks in the SM with the gauge group  $SU(3)_C$ , where  $C$  represents conservation  
 330 of color charge under  $SU(3)_C$  symmetry.  
 331 According to QFT, quarks can be treated as excitations of corresponding quark fields  $\psi$ .  
 332 Quark fields are invariant under  $SU(3)_C$  transformation

$$\psi \rightarrow e^{i\theta(x)T_a}\psi \tag{2.2}$$

where  $T_a$  are generators of  $SU(3)_C$ , represented as  $T_a = \lambda_a/2$  with  $\lambda_a$  being the eight Gell-Mann matrices.

The free Dirac Lagrangian

$$\mathcal{L}_0 = \bar{\psi}(i\gamma^\mu\partial_\mu - m)\psi \quad (2.3)$$

is invariant under global  $SU(3)$  symmetry, but not under local  $SU(3)_C$  symmetry. To establish invariance under local  $SU(3)_C$  symmetry, the gauge covariant derivative  $D_\mu$  is defined so that

$$D_\mu\psi = (\partial_\mu - ig_s G_\mu^a T_a)\psi, \quad (2.4)$$

where  $g_s = \sqrt{4\pi\alpha_s}$  is the QCD coupling constant,  $G_\mu^a(x)$  are the eight gluon fields that transform under  $SU(3)_C$  as

$$G_\mu^a \rightarrow e^{iT_a\theta_a(x)} \left( G_\mu^a + \frac{i}{g_s} \partial_\mu \theta_a(x) \right) e^{-iT_a\theta_a(x)} = G_\mu^a - \frac{1}{g_s} \partial_\mu \theta_a(x) - f_{abc} \theta_b(x) G_\mu^c, \quad (2.5)$$

and  $T_a$  are the generators of  $SU(3)_C$  defined as  $T_a = \lambda_a/2$  with  $\lambda_a$  being the eight Gell-Mann matrices.

Defining the gluon field strength tensor  $G_{\mu\nu}^a$  as

$$G_{\mu\nu}^a \equiv \partial_\mu G_\nu^a - \partial_\nu G_\mu^a - g_s f^{abc} G_\mu^b G_\nu^c, \quad (2.6)$$

where  $f^{abc}$  are the structure constants of  $SU(3)_C$ , the gauge invariant QCD Lagrangian is

$$\mathcal{L}_{\text{QCD}} = \bar{\psi}(i\gamma^\mu D_\mu - m)\psi - \frac{1}{4} G_{\mu\nu}^a G_a^{\mu\nu}, \quad (2.7)$$

345 which can be expressed in the form of

$$\mathcal{L}_{\text{QCD}} = \underbrace{-\frac{1}{4}G_{\mu\nu}^a G_a^{\mu\nu}}_{\text{gluon kinematics \& self-interaction}} + \underbrace{\bar{\psi}(i\gamma^\mu\partial_\mu - m)\psi}_{\text{quark kinematics}} + \underbrace{\bar{\psi}^i(g_s\gamma^\mu(T_a)_{ij}G_\mu^a)\psi^j}_{\text{quark-gluon interaction}}. \quad (2.8)$$

346 with  $i, j$  being the color indices with integer values from 1 to 3. The noncommutativity  
 347 of  $SU(3)_C$  gives rise to an additional term consisting of only gluon fields and gluon-gluon  
 348 interactions. Additionally, the Lagrangian also forces gluons to be massless to maintain  
 349 gauge invariance.

### 350 2.1.2.2 Electroweak theory

351 The electroweak interaction is the unified description of the weak interaction and electro-  
 352 magnetism under the  $SU(2)_L \times U(1)_Y$  symmetry group, where  $L$  represents the left-handed  
 353 chirality of the weak interaction and  $Y$  represents the weak hypercharge quantum number.  
 354 The quantum number associated with the weak chirality is the weak isospin  $I$ . The EW  
 355 quantum numbers are connected by the Gell-Mann-Nishijima relation

$$Q = I_3 + Y/2 \quad (2.9)$$

356 where  $Q$  is the electric charge and  $I_3$  is the third component of weak isospin  $I$ .  
 357 Fermions can have either left-handed or right-handed chirality, and can be divided into  
 358 left-handed doublets and right-handed singlets

$$\psi_L = \begin{pmatrix} \nu_e \\ e_L \end{pmatrix}, \begin{pmatrix} \nu_\mu \\ \mu_L \end{pmatrix}, \begin{pmatrix} \nu_\tau \\ \tau_L \end{pmatrix}, \begin{pmatrix} u_L \\ d_L \end{pmatrix}, \begin{pmatrix} c_L \\ s_L \end{pmatrix}, \begin{pmatrix} t_L \\ b_L \end{pmatrix} \quad (2.10)$$

$$\psi_R = e_R, \mu_R, \tau_R, u_R, d_R, c_R, s_R, t_R, b_R,$$

359 with the exception of neutrino which can only have left-handed chirality in the SM.

360 Both left-handed and right-handed fermion fields are invariant under  $U(1)_Y$  transformation

$$\psi \rightarrow e^{iY\theta(x)/2}\psi. \quad (2.11)$$

361 Similar to QCD, to establish invariance under local  $U(1)_Y$  symmetry, the  $U(1)_Y$  gauge

362 covariant derivative  $D_\mu$  is defined as

$$D_\mu\psi = \left(\partial_\mu - ig'\frac{Y}{2}B_\mu\right)\psi \quad (2.12)$$

363 where  $B_\mu(x)$  is a vector gauge field that transforms under  $U(1)_Y$  as

$$B_\mu \rightarrow B_\mu + \frac{1}{g'}\partial_\mu\theta(x) \quad (2.13)$$

364 and  $g'$  is the  $B_\mu$  coupling constant.

365 Right-handed fermion singlets are not affected by  $SU(2)_L$  transformation, so fermion fields

366 transform under  $SU(2)_L$  as

$$\psi_L \rightarrow e^{iI_3\vec{\theta}(x)\cdot\vec{\sigma}/2}\psi_L \quad (2.14)$$

$$\psi_R \rightarrow \psi_R.$$

367 where  $\vec{\sigma}/2$  are generators of  $SU(2)_L$  and  $\vec{\sigma}$  are Pauli matrices. In order to preserve local

368 symmetry, the gauge covariant derivative for  $SU(2)_L$  is defined as

$$D_\mu\psi_L = \left(\partial_\mu - ig\frac{\sigma_i}{2}W_\mu^i\right)\psi_L \quad (2.15)$$

369 where  $W_\mu^i(x)$  ( $i = 1, 2, 3$ ) are three boson gauge fields that transform under  $SU(2)_L$  as

$$W_\mu^i \rightarrow e^{i\frac{\sigma_i}{2}\theta_i(x)} \left( W_\mu^i + \frac{i}{g}\partial_\mu \right) e^{-i\frac{\sigma_i}{2}\theta_i(x)} = W_\mu^i + \frac{2}{g}\partial_\mu\theta_a(x) + \epsilon^{ijk}\theta_j(x)W_\mu^k, \quad (2.16)$$

370 with  $g$  as the gauge coupling constant for  $W_\mu^i$ , and  $\epsilon^{ijk}$  as the structure constant for  $SU(2)_L$ .

371 The gauge covariant derivative for  $SU(2)_L \times U(1)_Y$  can then be written as

$$\begin{aligned} D_\mu\psi_L &= \left( \partial_\mu - ig'\frac{Y_L}{2}B_\mu - ig\frac{\sigma_i}{2}W_\mu^i \right) \psi_L \\ D_\mu\psi_R &= \left( \partial_\mu - ig'\frac{Y_R}{2}B_\mu \right) \psi_R. \end{aligned} \quad (2.17)$$

372 Similar to QCD, the kinetic term is added by defining field strengths for the four gauge fields

$$\begin{aligned} B_{\mu\nu} &\equiv \partial_\mu B_\nu - \partial_\nu B_\mu \\ W_{\mu\nu}^i &\equiv \partial_\mu W_\nu^i - \partial_\nu W_\mu^i - ge^{ijk}W_\mu^j W_\nu^k. \end{aligned} \quad (2.18)$$

373 The local  $SU(2)_L \times U(1)_Y$  invariant EW Lagrangian can then be expressed as

$$\begin{aligned} \mathcal{L}_{\text{EW}} &= i\bar{\psi}(\gamma^\mu D_\mu)\psi - \frac{1}{4}W_{\mu\nu}^i W_i^{\mu\nu} - \frac{1}{4}B_{\mu\nu}B^{\mu\nu} \\ &= \underbrace{i\bar{\psi}(\gamma^\mu \partial_\mu)\psi}_{\text{fermion kinematics}} - \underbrace{\bar{\psi} \left( \gamma^\mu g' \frac{Y}{2} B_\mu \right) \psi - \bar{\psi}_L \left( \gamma^\mu g \frac{\sigma_i}{2} W_\mu^i \right) \psi_L}_{\text{fermion-gauge boson interaction}} - \underbrace{\frac{1}{4}W_{\mu\nu}^i W_i^{\mu\nu} - \frac{1}{4}B_{\mu\nu}B^{\mu\nu}}_{\text{boson kinematics \& self-interaction}}. \end{aligned} \quad (2.19)$$

374 Under  $\approx 159.5$  GeV, the EW symmetry  $SU(2)_L \times U(1)_Y$  undergoes spontaneous symme-  
 375 try breaking into  $U(1)_{\text{QED}}$  symmetry, which corresponds to a separation of the weak and  
 376 electrodynamic forces. This replaces the massless and similarly-behaved EW gauge bosons  
 377  $B_\mu$  and  $W_\mu^i$  with the EM boson  $\gamma$  and the weak bosons  $Z/W^\pm$ . Additionally, electroweak  
 378 spontaneous symmetry breaking also gives  $Z$  and  $W^\pm$  masses via the Higgs mechanism, dis-

379 cussed in Section 2.1.2.3. The spontaneous symmetry breaking leads to reparameterization  
 380 of  $B_\mu$  and  $W_\mu^i$  to  $W^\pm/Z/\gamma$  bosons via a specific choice of gauge for the Higgs field

$$\begin{aligned} W_\mu^\pm &\equiv \frac{1}{\sqrt{2}} \left( W_\mu^1 \mp i W_\mu^2 \right) \\ \begin{pmatrix} A_\mu \\ Z_\mu \end{pmatrix} &\equiv \begin{pmatrix} \cos \theta_W & \sin \theta_W \\ -\sin \theta_W & \cos \theta_W \end{pmatrix} \begin{pmatrix} B_\mu \\ W_\mu^3 \end{pmatrix} \end{aligned} \quad (2.20)$$

381 where  $\theta_W \equiv \cos^{-1} \left( g / \sqrt{g^2 + g'^2} \right)$  is the weak mixing angle. The boson kinetic term can also  
 382 be refactorized to extract cubic (three vertices) and quartic (four vertices) self-interactions  
 383 among the gauge bosons [4]. The Lagrangian can then be rewritten as

$$\begin{aligned} \mathcal{L} &= \underbrace{e A_\mu \bar{\psi} (\gamma^\mu Q) \psi}_{\text{electromagnetism}} + \underbrace{\frac{e}{2 \sin \theta_W \cos \theta_W} \bar{\psi} \gamma^\mu (v_f - a_f \gamma_5) \psi Z_\mu}_{\text{neutral current interaction}} \\ &+ \underbrace{\frac{g}{2\sqrt{2}} \sum_{\psi_L} [\bar{f}_2 \gamma^\mu (1 - \gamma_5) f_1 W_\mu^+ + \bar{f}_1 \gamma^\mu (1 - \gamma_5) f_2 W_\mu^-]}_{\text{charged current interaction}} \\ &+ \mathcal{L}_{\text{kinetic}} + \underbrace{\mathcal{L}_{\text{cubic}} + \mathcal{L}_{\text{quartic}}}_{\text{boson self-interaction}} \end{aligned} \quad (2.21)$$

384 where  $\gamma_5 = i\gamma^0\gamma^1\gamma^2\gamma^3$  is the chirality projection operator,  $a_f = I_3$ ,  $v_f = I_3(1 - 4|Q| \sin^2 \theta_W)$   
 385 and  $f_1, f_2$  are up and down type fermions of a left-handed doublet.

### 386 2.1.2.3 Higgs mechanism

387 So far, the EW bosons are massless, since the mass terms  $-m\bar{\psi}\psi$  for fermions and  $-mA^\mu A_\mu$   
 388 for bosons are not invariant under the EW Lagrangian. The particles must then acquire  
 389 mass under another mechanism. The Brout-Engler-Higgs mechanism [5–7] was introduced



390 in 1964 to rectify this issue, and verified in 2012 with the discovery of the Higgs boson [8, 9].

391 The Higgs potential is expressed as

$$V(\phi^\dagger\phi) = \mu^2\phi^\dagger\phi + \lambda(\phi^\dagger\phi)^2 \quad (2.22)$$

392 where  $\mu^2$  and  $\lambda > 0$  are arbitrary parameters, and the  $SU(2)_L$  doublet  $\phi$  is the Higgs field

$$\phi = \begin{pmatrix} \phi^+ \\ \phi^0 \end{pmatrix}, \quad (2.23)$$

393 with complex scalar fields  $\phi^+$  and  $\phi^0$  carrying +1 and 0 electric charge respectively. The

394 Lagrangian for a scalar field is

$$\mathcal{L}_H = (\partial_\mu\phi)^\dagger (\partial^\mu\phi) - V(\phi^\dagger\phi). \quad (2.24)$$

395 Since the potential  $V(\phi^\dagger\phi)$  is constrained by  $\lambda > 0$ , the ground state is solely controlled by

396  $\mu$ . If  $\mu^2 > 0$ , the ground state would be  $\phi = 0$ , and the EW bosons would remain massless.

397 If  $\mu^2 < 0$ , the ground state would be

$$|\phi|^2 = -\frac{\mu^2}{2\lambda} \equiv \frac{v^2}{\sqrt{2}}, \quad (2.25)$$

398 where  $v$  is defined as the vacuum expectation value (VEV). The standard ground state for

399 the Higgs potential without loss of generality can be chosen as

$$\phi(0) = \frac{1}{\sqrt{2}} \begin{pmatrix} 0 \\ v \end{pmatrix}. \quad (2.26)$$

### sombrero potential pic

Having  $U(1)$  symmetry allows any  $-e^{i\theta}\sqrt{\mu^2/\lambda}$  to be a ground state energy for the Higgs Lagrangian. This degeneracy results in spontaneous symmetry breaking of the  $SU(2)_L \times U(1)_Y$  symmetry into  $U(1)_{\text{QED}}$  symmetry when the Higgs field settles on a specific vacuum state as a result of a perturbation or excitation. The spontaneous symmetry breaking introduces three massless (Nambu-Goldstone) vector gauge boson  $\xi$  and a massive scalar boson  $\eta$ , each corresponds to a generator of the gauge group. The bosons can be extracted using the reparameterization [10]

$$\xi \equiv \phi^+ \sqrt{2}, \quad \eta \equiv \phi^0 \sqrt{2} - v, \quad (2.27)$$

400 such that  $\xi, \eta$  are real fields. The Higgs field now become

$$\phi = \frac{v + \eta + i\xi}{\sqrt{2}} = e^{i\xi \cdot \frac{\sigma}{2v}} \begin{pmatrix} 0 \\ \frac{v + \eta}{\sqrt{2}} \end{pmatrix}. \quad (2.28)$$

401 Due to  $U(1)_{\text{EM}}$  invariance, a unitary gauge with the transformation  $\phi \rightarrow \exp(-i\xi \cdot \frac{\sigma}{2v})$  can  
 402 be chosen to eliminate the massless bosons and incorporate them into the EM and weak  
 403 bosons through the reparameterization in Equation 2.20. This leaves the massive  $\eta$  which  
 404 can now be observed as an excitation of the Higgs field and consequently is the Higgs boson  
 405  $h$ . Using the EW covariant derivative from Equation 2.17, the Higgs Lagrangian around the  
 406 vacuum state becomes

$$\begin{aligned} \mathcal{L}_H &= (D_\mu \phi)^\dagger (D^\mu \phi) - \mu^2 \left( \frac{v + h}{\sqrt{2}} \right)^2 - \lambda \left( \frac{v + h}{\sqrt{2}} \right)^4 \\ &= (D_\mu \phi)^\dagger (D^\mu \phi) - \frac{1}{2} \mu^2 h^2 - \lambda v h^3 - \frac{\lambda}{4} h^4 - \dots \end{aligned} \quad (2.29)$$

407 The Higgs mass can be extracted from the quadratic term as  $m_H = \sqrt{-2\mu^2}$ . The kinetic  
 408 term in the Lagrangian can be written as

$$\begin{aligned} (D_\mu \phi)^\dagger (D^\mu \phi) &= \frac{1}{2}(\partial_\mu h)^2 + \frac{g^2}{8}(v+h)^2 |W_\mu^1 - iW_\mu^2|^2 + \frac{1}{8}(v+h)^2 (g'W_\mu - gB_\mu)^2 \\ &= \frac{1}{2}(\partial_\mu h)^2 + (v+h)^2 \left( \frac{g^2}{4} W_\mu^+ W^{-\mu} + \frac{1}{8} (g^2 + g'^2) Z_\mu^0 Z^{0\mu} \right). \end{aligned} \quad (2.30)$$

409 Masses for the EW bosons can be extracted from the quadratic terms

$$m_{W^\pm} = \frac{v}{2}g, \quad m_Z = \frac{v}{2}\sqrt{g^2 + g'^2}, \quad m_\gamma = 0. \quad (2.31)$$

410 The fermion mass term  $-m\bar{\psi}\psi$  still breaks EW invariance after spontaneous symmetry  
 411 breaking. Fermions instead acquire mass by replacing the mass term with a gauge invariant  
 412 Yukawa term in the EW Lagrangian for fermions' interactions with the Higgs field [10]

$$\begin{aligned} \mathcal{L}_{\text{Yukawa}} &= -c_f \frac{v+h}{\sqrt{2}} (\bar{\psi}_R \psi_L + \bar{\psi}_L \psi_R) \\ &= - \underbrace{\frac{c_f}{\sqrt{2}} v (\bar{\psi}\psi)}_{\text{fermion mass}} - \underbrace{\frac{c_f}{\sqrt{2}} (h\bar{\psi}\psi)}_{\text{fermion-Higgs interaction}}, \end{aligned} \quad (2.32)$$

413 where  $c_f$  is the fermion-Higgs Yukawa coupling. The fermion mass is then  $m_f = c_f v / \sqrt{2}$ .

## 414 2.2 Beyond the Standard Model

### 415 2.2.1 Top-philic vector resonance

416 Many BSM models extend the SM by adding to the SM gauge group additional  $U(1)'$  gauge  
 417 symmetries, each with an associated vector gauge boson nominally named  $Z'$  [11]. In the case

418 of a BSM global symmetry group with rank larger than the SM gauge group, the symmetry  
 419 group can break into  $G_{\text{SM}} \times U(1)'^n$ , where  $G_{\text{SM}}$  is the SM gauge group  $SU(3)_C \times SU(2)_L \times$   
 420  $U(1)_Y$  and  $U(1)'^n$  is any  $n \geq 1$  number of  $U(1)'$  symmetries. The existence of additional  
 421 vector bosons  $Z'$  would open up many avenues of new physics e.g. extended Higgs sectors  
 422 from  $U(1)'$  symmetry breaking, existence of flavor-changing neutral current (FCNC) effects  
 423 in some models, and possible exotic production from heavy  $Z'$  decays [11].  
 424 Due to the top quark having the largest mass out of all known elementary particles in the SM,  
 425 many BSM models [12–15] predict 'top-philic' vector resonances that have much stronger  
 426 coupling to the top quark compared to other quarks such that the coupling factors to lighter  
 427 quarks are negligible.  
 428 The analysis in this thesis attempts to reconstruct a top-philic  $Z'$  resonance directly to avoid  
 429 dependency on model choice. Previous model-independent BSM  $t\bar{t}t\bar{t}$  search [16] in the single-  
 430 lepton final state and similar mass ranges showed no significant excess with upper limits on  
 431 observed (expected)  $Z'$  production cross section between 21 (14) fb to 119 (86) fb depending  
 432 on parameter choice. In addition, a simplified color-singlet vector particle model [16, 17] is  
 433 employed to study model-dependent interpretations. The interaction Lagrangian assumes  
 434 only coupling with the top quark and has the form

$$\begin{aligned}
 \mathcal{L}_{Z'} &= \bar{t}\gamma_\mu (c_L P_L + c_R P_R) t Z'^\mu \\
 &= c_t \bar{t}\gamma_\mu (\cos \theta P_L + \sin \theta P_R) t Z'^\mu,
 \end{aligned}
 \tag{2.33}$$

435 where  $c_t = \sqrt{c_L^2 + c_R^2}$  is the top coupling strength,  $P_{L/R} = (1 \mp \gamma_5)/2$  are the chirality  
 436 projection operators, and  $\theta = \tan^{-1}(c_R/c_L)$  is the chirality mixing angle [16]. Expanding

the Lagrangian results in

$$\mathcal{L}_{Z'} = \frac{1}{\sqrt{2}} \bar{t} \gamma_\mu \left[ \sin \left( \theta + \frac{\pi}{4} \right) - \left( \sqrt{2} \cos \left( \theta + \frac{\pi}{4} \right) \right) \gamma_5 \right] t Z'^\mu, \quad (2.34)$$

which bears striking resemblance to the EW Lagrangian neutral current interaction term in Equation 2.21, showing the similarity between the  $Z'$  and the neutral  $Z$  boson which acquires mass as a result of  $SU(2)_L \times U(1)_Y$  spontaneous symmetry breaking.

Assuming the  $Z'$  mass  $m_{Z'}$  is much larger than the top mass ( $m_t^2/m_{Z'}^2 \approx 0$ ), the  $Z'$  decay width at leading-order (LO) can be approximated as

$$\Gamma(Z' \rightarrow t\bar{t}) \approx \frac{c_t^2 m_{Z'}}{8\pi}. \quad (2.35)$$

It can be observed that  $\Gamma/m_{Z'} \approx c_t^2/8\pi \ll 1$  for  $c_t \approx 1$ . This suggests a very narrow and well-defined resonance peak, which validates the narrow-width approximation for choice of  $c_t = 1$  and supports efforts to directly reconstruct the resonance.

The main production channels for the aforementioned heavy top-philic color singlet  $Z'$  are at tree level and loop level, with the one-loop level being the dominant processes. Loop level processes are dependent on the chirality angle  $\theta$ , where  $\theta = \pi/4$  suppresses all but gluon-initiated box subprocesses [16]. To minimize model dependence, only the tree level production was considered and consequently  $\theta = \pi/4$  was chosen for this analysis. The Feynman diagrams for tree level production channels are shown in Figure 2.3.

The single-top associated final states  $tjZ'$  and  $tWZ'$  productions are suppressed by three-body phase space, resulting in smaller cross sections, by a factor of two, compared to the top pair associated final state process  $t\bar{t}Z' \rightarrow t\bar{t}t\bar{t}$ . Unlike  $tjZ'$  and  $tWZ'$  which are produced by

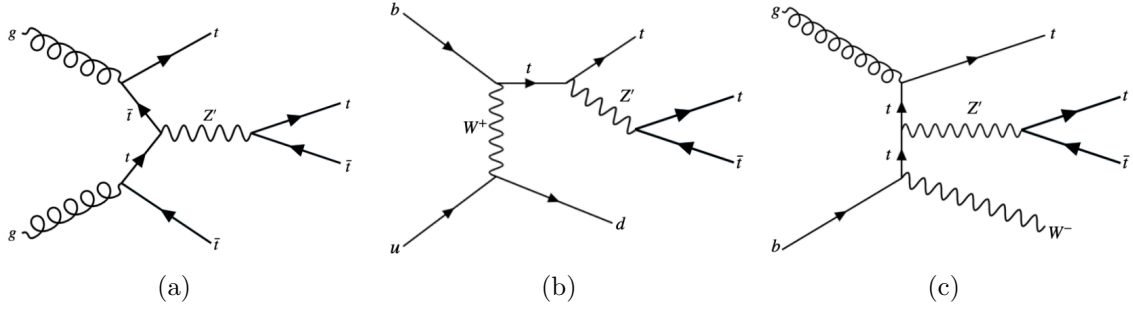


Figure 2.3: tree level  $Z'$  production in association with (a)  $t\bar{t}$  to 4tops, (b)  $tj$  (light quark) to 3tops, (c)  $tW$  to 3 tops, derived from top quark final states produced via strong, EW and mixed QCD-EW interactions [16]

EW and mixed QCD-EW interactions respectively,  $t\bar{t}t\bar{t}$  production is governed by the strong interaction only which can overpower phase space suppression. Additionally, unlike  $t\bar{t}t\bar{t}$  production which is independent of  $\theta$ , single-top associated processes are minimally suppressed under pure left-handed interaction ( $\theta = 0$ ) and maximally suppressed under pure right-handed interaction ( $\theta = \pi/2$ ).

## 2.2.2 BSM four-top quark production

The analysis presented in this thesis uses the  $t\bar{t}t\bar{t}$  final state signal signature to search for the existence of a heavy BSM resonance that couples strongly to the top quark. Cross section for  $t\bar{t}t\bar{t}$  production can be enhanced by many possible BSM models, in particular possible production of a heavy neutral resonance boson  $X$ , decaying to a  $t\bar{t}$  pair, in association with a  $t\bar{t}$  pair in composite Higgs scenarios (citations) or two-Higgs-doublet-model (2HDM!). The  $t\bar{t}X$  production mode and consequently  $t\bar{t}t\bar{t}$  signal signature can provide a more sensitive channel for searches by avoiding contamination from the large  $gg \rightarrow t\bar{t}$  SM background in an inclusive  $X \rightarrow t\bar{t}$  search.

## Decay modes

The different  $W$  boson decay modes shown in Figure 2.2 result in many different final states for  $t\bar{t}X/t\bar{t}t\bar{t}$  decay, which can each be classified into one of three channels: all hadronic decays; exactly one lepton or two opposite-sign leptons (1LOS); exactly two same-sign leptons or three or more leptons (SSML). The branching ratio for each channel is shown in Figure 2.4. The all hadronic and 1LOS channels have much larger branching ratios compared to SSML channel but suffer heavily from irreducible  $gg \rightarrow t\bar{t}$  background contamination, giving SSML channel better sensitivity at the cost of lower statistics. This is also the targeted channel for the analysis in this thesis.

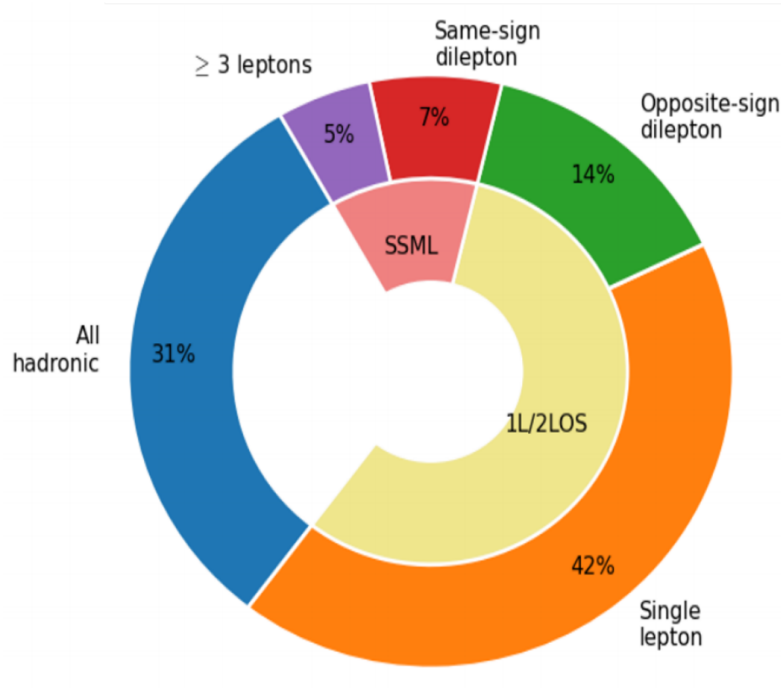


Figure 2.4: Caption

## Chapter 3. LHC & ATLAS Experiment

### 3.1 The Large Hadron Collider

theoretical predictions are tested with experimental data obtained from particle accelerators world's largest accelerator built by CERN situated on the border of Switzerland and France has been operating since xxxx lifetime divided into 3 runs, currently on Run 3 with planned upgrades on the horizon responsible for a number of discoveries aka Higgs, etc.

#### 3.1.1 Overview

[Basic info: location, size, main working mechanism, main detectors, main physics done]  
- 27 km circumference, reusing LEP tunnels 175 m below ground level  
- 7-13-13.6 TeV center of mass energies for pp collisions  
- other than pp, also collides pPb, PbPb at 4 points with 4 main detectors: ATLAS, CMS (general purpose detectors), ALICE (heavy ion physics, ion collisions), LHCb (*b*-physics)

#### 3.1.2 LHC operations

- focuses mainly on pp collisions for this thesis - beams split into bunches of  $1.1 \times 10^{11}$  protons with instantaneous luminosity of up to  $2 \times 10^{34} \text{ cm}^{-2}\text{s}^{-1}$   
- beam energies ramp up in other accelerators before injection, full ramp up to 6.5 GeV about 20 minutes  
(insert full diagram of accelerator chain)  
Linac 4: hydrogen atoms, accelerated up to 160 MeV



PSB: H atoms stripped of electrons before injection, accelerated to 2 GeV

PS: 26 GeV, SPS: 450 GeV

LHC: injection in opposite directions, 6.5 TeV per beam

Run 1: 2010-2012, Run 2: 2015-2018, Run 3: 2022-2025, HL-LHC: 2029-?

COM energies: 7 & 8 TeV, 13 TeV, 13.6 TeV, 13.6 & 14 TeV

inbetween periods: long shutdowns (LS1, LS2, LS3)

## Physics at the LHC

### 3.2 The ATLAS detector

multipurpose particle detector with a symmetric cylindrical geometry and a solid angle

coverage of almost  $4\pi$

44m long, 25m diameter

inner detector, solenoid/toroid magnet, EM & hadronic calorimeters, muon spectrometer

(insert figure)

right-handed cylindrical system, z-axis follows beamline, azimuthal and polar (0 in the beam direction) angles measured with respect to beam axis.

pseudorapidity  $\eta = -\ln \tan(\theta/2)$ , approaches  $\pm \infty$  along and 0 orthogonal to the beamline

distance  $\Delta R = \sqrt{\Delta\eta^2 + \Delta\phi^2}$

transverse energy  $E_T = \sqrt{p_T^2 + m^2}$

transverse momentum  $p_T$  component of momentum orthogonal to the beam axis  $p_T =$

# Standard Model Production Cross Section Measurements

Status: October 2023

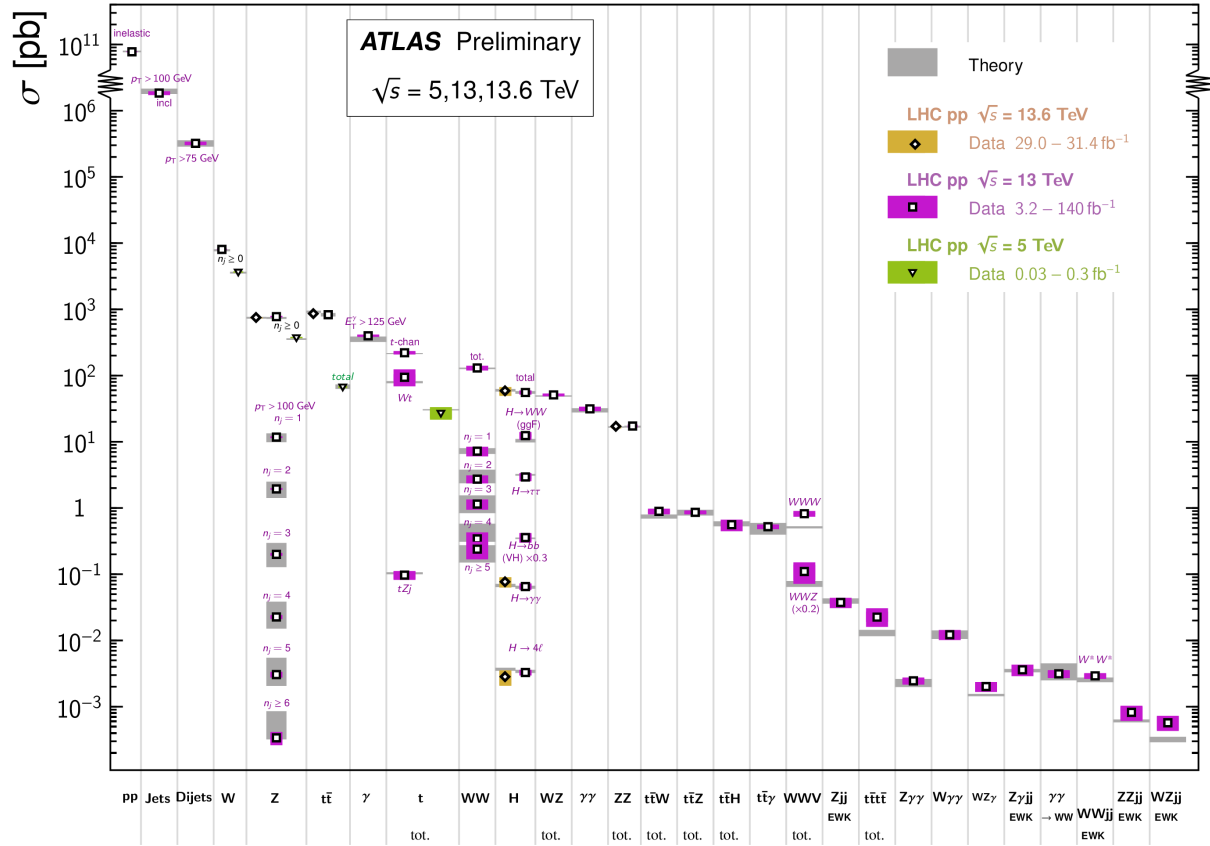


Figure 3.1: Caption [18]

520  $\sqrt{p_x^2 + p_y^2}$

### 521 3.2.1 Inner detector

522 • measures tracks of charged particles with high momentum resolution ( $\sigma_{p_T}/p_T =$   
 523  $0.05\% \pm 1\%$ )

524 • covers particles with  $p_T > 0.5$  GeV,  $|\eta| < 2.5$

525 pixel detector -> semiconductor tracker -> transition radiation tracker, innermost to  
 526 outermost

527 • pixel detector:

528 – innermost, 250  $\mu\text{m}$  silicon pixel layers

529 – detects charged particles from electron-hole pair production in silicon

530 – measures impact parameter resolution & vertex identification for reconstruction  
 531 of short-lived particles

532 – spatial resolution of 10  $\mu\text{m}$  in the  $R - \phi$  plane and 115  $\mu\text{m}$  in the z-direction

533 – 80.4m readout channels

534 • sct:

535 – surrounds pixel detector, silicon microstrip layers with 80  $\mu\text{m}$  strip pitch

536 – particle tracks cross 8 strip layers

537 – measures particle momentum, impact parameters, vertex position

538 – spatial resolution of 17  $\mu\text{m}$  in the  $R - \phi$  plane and 580  $\mu\text{m}$  in the z-direction

539 – 6.3m readout channels.

• trt:

- outermost, layers of 4 mm diameter gaseous straw tubes with transition radiation material (70%  $Xe$  + 27%  $CO_2$  + 3%  $O_2$ ) & 30  $\mu m$  gold-plated wire in the center
- tubes 144 cm length in barrel region ( $|\eta| < 1$ ), 37 cm in the endcap region ( $1 < |\eta| < 2$ ), arranged in wheels instead of parallel to beamline)
- gas mixture produces transition radiation when ionized for electron identification
- resolution/accuracy of 130  $\mu m$  for each straw tube in the  $R - \phi$  plane
- 351k readout channels

### 3.2.2 Calorimeter systems

surrounds the inner detector & solenoid magnet, covers  $|\eta| < 4.9$  and full  $\phi$  range. Alternates passive and active material layers. Incoming particles passing through calorimeter produce EM cascades or hadronic showers in passive layer. Energies deposited and convert to electric signals in active layers for readout.

EM calorimeter:

- innermost, lead-LAr detector (passive-active)

- measures EM cascades (bremsstrahlung & pair production) produced by electrons/photons

- divided into barrel region ( $|\eta| < 1.475$ )

& endcap regions ( $1.375 < |\eta| < 3.2$ )

with transition region ( $1.372 < |\eta| < 1.52$ ) containing extra cooling materials for inner detector

- end-cap divided into outer wheel ( $1.372 < |\eta| < 2.5$ ) & inner wheel ( $2.5 < |\eta| < 3.2$ )

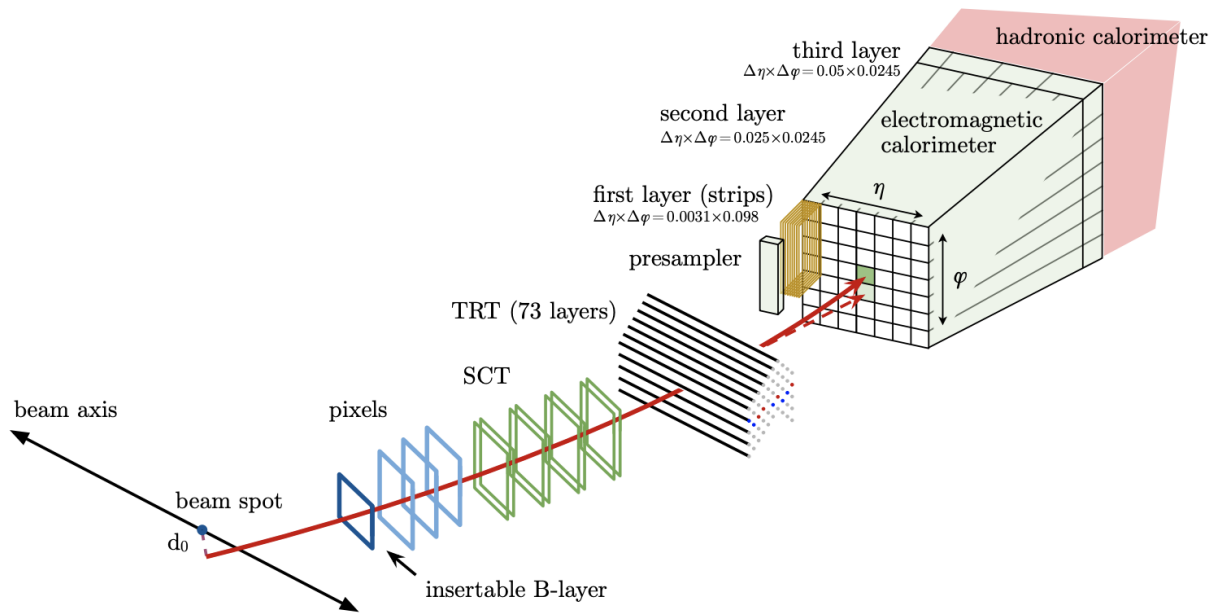


Figure 3.2: Caption [19]

- higher granularity in ID ( $|\eta| < 2.5$ ) range for electrons/photons & precision physics, coarser elsewhere for jet reconstruction & MET measurements
- split into tile calorimeter in barrel region ( $|\eta| < 1.0$ ) & extended barrel region ( $0.8 < |\eta| < 1.7$ ), LAr hadronic end-cap calorimeter (HEC) in end-cap regions ( $1.5 < |\eta| < 3.2$ ) & LAr forward calorimeters (FCal) in  $3.1 < |\eta| < 4.9$  range.
- outermost
- measures hadronic showers from inelastic QCD collisions
- thick enough to prevent most particles showers from reaching muon spectrometer
- tile calorimeters: steel-plastic scintillating tiles, readout via photomultiplier tubes
- hec: behind tile calorimeters, 2 wheels per end-cap. copper plates-

LAr. overlap with other calorimeters – fcal: 1 copper module & 2 tungsten modules-LAr. copper optimized for EM measurements, tungsten for hadronic.

### 3.2.3 Muon spectrometer

- ATLAS outermost layer. measures muon momenta & charge in range  $|\eta| < 2.7$
- momentum measured by deflection in track from toroid magnets producing magnetic field orthogonal to muon trajectory
  - large barrel toroids in  $|\eta| < 1.4$ , strength 0.5 T
  - 2 smaller end-cap toroids in  $1.6 < |\eta| < 2.7$ , strength 1 T
  - transition region  $1.4 < |\eta| < 1.6$ , deflection provided by a combination of barrel and end-cap magnets
- chambers installed in 3 cylindrical layers, around the beam axis in barrel region & in planes perpendicular to beam axis in the transition and end-cap regions
- split into high-precision tracking chambers (monitored drift tubes & cathode strip chambers) & trigger chambers (resistive plate chambers & thin gap chambers)
- trigger chambers provide fast muon multiplicity & approximate energy range information with L1 trigger logic

– mdt:  $|\eta| < 2.0$

\* range  $|\eta| < 2.7$ , innermost layer \* precision momentum measurement

615 ment 638

616 \* layers of 30 mm drift tubes filled 639

617 with 93% *Ar* & 7% *CO*<sub>2</sub>, with

618 a 50 μm gold-plated tungsten-

619 rhenium wire at the center

620 \* muons pass through tube, ion-

621 izing gas and providing signals.

622 Combining signals from tubes

623 forms track

624 \* maximum drift time from wall

625 to wire 700 ns

626 \* resolution: 35 μm per chamber,

627 80 μm per tube

628 — CSC:

629 \* forward region  $2.0 < |\eta| < 2.7$ ,

630 highest particle flux and density

631 region

632 \* multiwire proportional chambers

633 with higher granularity, filled

634 with 80% *Ar* & 20% *CO*<sub>2</sub> 640

635 \* shorter drift time than MDT<sub>1</sub>

636 plus other features making CSC

637 suitable for high particle densities

sities and consequently able to  
handle background conditions

\* resolution: 40 μm in bending  $\eta$ -  
plane, 5 mm in nonbending  $\phi$ -  
plane due to coarser cathode seg-  
mentation, per CSC plane

644       – rpc:

645           \* range  $|\eta| < 1.05$

646           \* provide fast meas

647       – tgc:

648           \* range  $1.05 < |\eta| < 2.7$

### 649   **3.2.4   Forward detectors**

- 650       • LUCID (LUminosity measurement using Cherenkov Integrating Detector):  $\pm 17$  m from  
651       interaction point, measures luminosity using  $pp$  scattering in the forward region
- 652       • ALFA (Absolute Luminosity for ATLAS):  $\pm 240$  m, measures  $pp$  scattering at small  
653       angles
- 654       • ZDC (Zero-Degree Calorimeter):  $\pm 140$  m, measures centrality in heavy-ion collisions

### 655   **3.2.5   Magnetic systems**

656   superconducting solenoid & toroid magnets cooled to 4.5 K with liquid helium

657   solenoid: 2.56 m diameter, 5.8 m length, 2 T strength axial magnetic field, encloses inner  
658   detector

659   toroid = barrel + endcap toroid x2

660   barrel toroid: 9.2/20.1 m inner/outer diameter, 25.3 m length, 0.5 T strength

661   endcap toroid: 1.65/10.7 m inner/outer diameter, 5 m length, 1 T strength

662   (show magnet system diagram)

### 663   **3.2.6   Trigger & data acquisition**

664   LHC produces large amount of data (40 MHz with 25 ns bunch crossing), necessitates a way  
665   to filter out trash from interesting events



handles online processing, selecting and recording interesting events for further offline processing and more in-depth analyses

- Level-1 (L1) trigger: online, fast hardware-based trigger, reduces to 100 kHz
  - L1 calorimeter triggers (L1Calo): selects high energy objects & MET
  - L1 muon triggers (L1Muon): selects using hit information from RPC & TGC
  - L1 topological trigger (L1Topo): select based on topological selection synthesized using information from L1Calo & L1Muon
  - Central Trigger Processor (CTP): uses L1Calo/Muon/Topo for final L1 trigger decision within  $2.5 \mu\text{s}$  latency. Also identify regions of interest in  $\eta$  and  $\phi$  to be processed directly by HLT
- L1 trigger information read out by Front-End (FE) detector electronics then sent to ReadOut Drivers (ROD) for preprocessing and subsequently to ReadOut System (ROS) to buffer
- High-Level Trigger (HLT): offline, software-based trigger, using dedicated algorithms and L1 output as input, reduces to 1 kHz
- Send to storage for analyses after HLT

overall trigger process reduces original collision data rate by a factor of about 10000 after HLT  
(show TDAQ diagram)

# Chapter 4. Particle Reconstruction & Identification

Activity within the ATLAS detector are recorded as raw electronic signals, which can be utilized by ATLAS reconstruction software to derive physics objects for analysis. This chapter describes the reconstruction and identification of basic objects (e.g. interaction vertices, tracks, topological clusters of energy deposits) and subsequently of complex physics objects i.e. particles and particle signatures.

## 4.1 Primary reconstruction

### 4.1.1 Tracks

Charged particles traveling through the ATLAS detector deposit energy in different layers of the ID and MS. The ID track reconstruction software consists of two algorithm chains: inside-out and outside-in track reconstruction [20–22].

The inside-out algorithm is primarily used for the reconstruction of primary particles i.e. particles directly produced from  $pp$  collisions or decay products of short-lived particles. The process starts by forming space points from seeded hits in the silicon detectors within the pixel & SCT detectors. Hits further away from the interaction vertex are added to the track candidate using a combinatorial Kalman filter [23] pattern recognition algorithm. Track candidates are then fitted with a  $\chi^2$  filter [24] and loosely matched to a fixed-sized EM cluster. Successfully matched track candidates are re-fitted with a Gaussian-sum filter (GSF) [25], followed by a track scoring strategy to resolve fake tracks & hit ambiguity

between different tracks [26]. The track candidate is then extended to the TRT to form final tracks satisfying  $p_T > 400$  MeV. The outside-in algorithm handles secondary tracks mainly produced from long-lives particles or decays of primary particles by back-tracking from TRT segments, which are then extended inward to match silicon hits in the pixel and SCT detectors to form track reconstruction objects.

### 4.1.2 Vertices

Vertices represent the point of interaction or decay for particles within the ATLAS detector. Primary vertices (PVs) are defined as the point of collision for hard-scattering  $pp$  interactions, while secondary or displaced vertices result from particle decays occurring at a distance from its production point.

Reconstruction of PVs is crucial to accurately profile the kinematic information of an event and form a basis for subsequent reconstruction procedures. Primary vertex reconstruction occurs in two stages: vertex finding and vertex fitting [27]. The vertex finding algorithm uses the spatial coordinates of reconstructed tracks to form the seed for a vertex candidate. An adaptive vertex fitting algorithm [28] then iteratively evaluates track-vertex compatibility to estimate a new best vertex position. Less compatible tracks are down-weighted in each subsequent iteration, and incompatible tracks are removed and can be used for another vertex seed; the process is repeated until no further PV can be found. All reconstructed vertices without at least two matched tracks are considered invalid and discarded.

Secondary vertex reconstruction uses the Secondary Vertex Finder (SVF) algorithm [29] which is primarily designed to reconstruct  $b$ - and  $c$ -hadrons for flavor tagging purposes. The SVF aims to reconstruct one secondary vertex per jet and only considers tracks that

are matched to a two-track vertex and contained within a  $p_T$ -dependent cone around the jet axis. The tracks are then used to reconstruct a secondary vertex candidate using an iterative process similar to the PV vertex fitting procedure.

## Pile-up

At high luminosities, multiple interactions can be associated with one bunch crossing, resulting in many PVs. The effect is called pile-up, and usually result from soft QCD interactions. Pile-up can be categorized into two types: in-time pile-up, stemming from additional  $pp$  collisions in the same bunch crossing that is not the hard-scatter process; out-of-time pile-up, resulting from leftover energy deposits in the calorimeters from other bunch crossings.

### 4.1.3 Topological clusters

Topological clusters (topo-clusters) [30] consist of clusters of spatially related calorimeter cell signals. Topo-clusters are primarily used to reconstruct hadron- and jet-related objects in an effort to extract signal while minimizing electronic effects and physical fluctuations, and also allow for recovery of energy lost through bremsstrahlung or photon conversions. Cells with signal-to-noise ratio  $\varsigma_{\text{cell}}^{\text{EM}}$  passing a primary seed threshold are seeded into a dynamic topological cell clustering algorithm as part of a proto-cluster. Neighboring cells satisfying a cluster growth threshold are collected into the proto-cluster. If a cell is matched to two proto-clusters, the clusters are merged. Two or more local signal maxima in a cluster satisfying  $E_{\text{cell}}^{\text{EM}} > 500$  MeV suggest the presence of multiple particles in close proximity, and the cluster is split accordingly to maintain good resolution of the energy flow. The process continues iteratively until all cells with  $\varsigma_{\text{cell}}^{\text{EM}}$  above a principal cell filter level have been matched to a cluster.

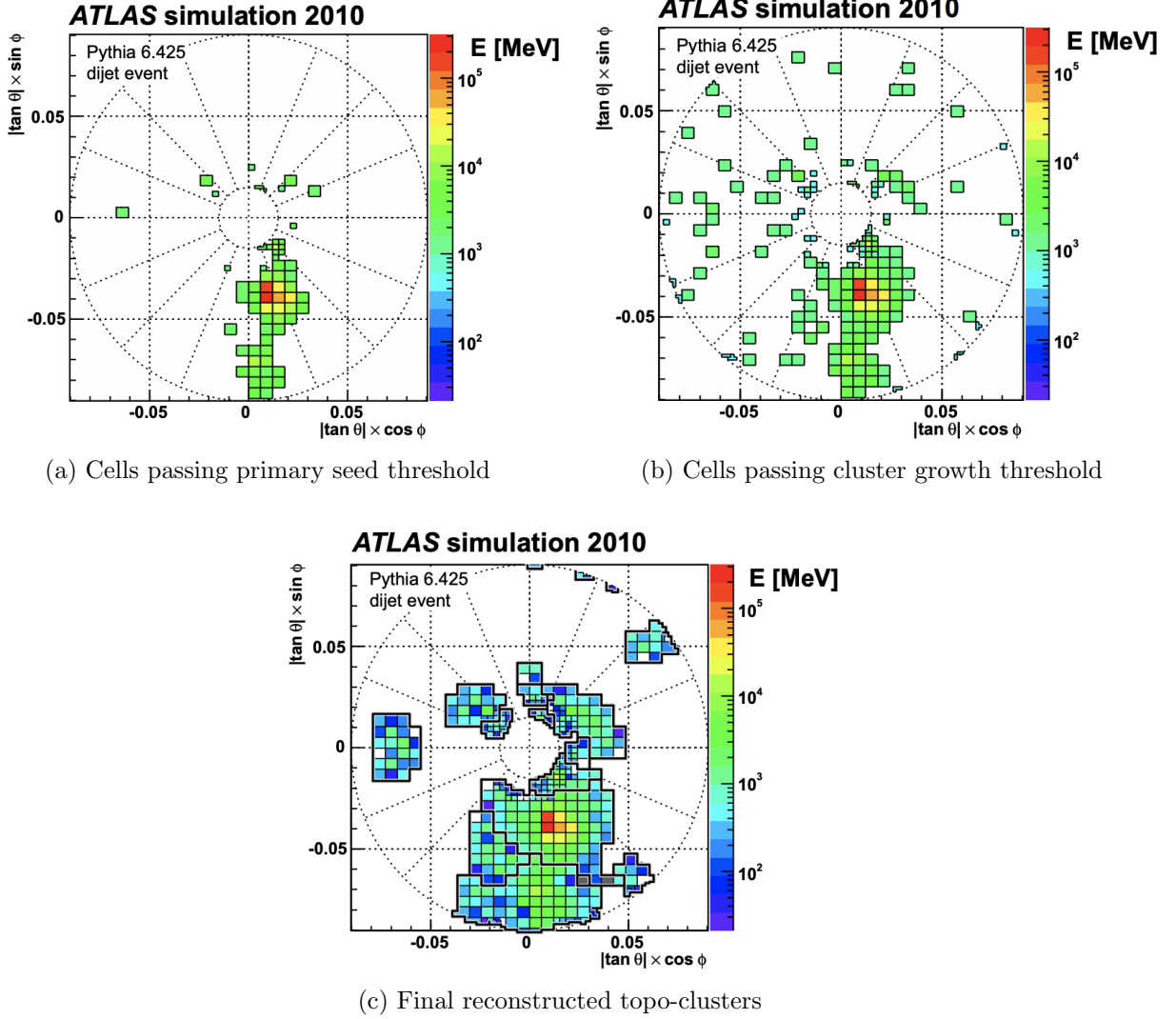


Figure 4.1: Stages of topo-cluster formation corresponding to each threshold. In (a), proto-clusters are seeded from cells with adequate signal significance  $\zeta_{\text{cell}}^{\text{EM}}$ . The clusters are further merged and split in (b) following a predefined cluster growth threshold. The process stops in (c) when all sufficiently significant signal hits have been matched to a cluster [30].

## 4.2 Jets

Quarks, gluons and other hadrons with non-neutral color charge cannot be observed individually due to QCD color confinement, which forces a non-color-neutral hadron to almost immediately undergo hadronization, producing a collimated cone of color-neutral hadrons defined as a jet. Jet signals can be used to reconstruct and indirectly observe the quarks or gluons from which the jet originated in the original hard-scattering process.

### 4.2.1 Jet reconstruction

The ATLAS jet reconstruction pipeline is largely carried out using a particle flow (PFlow) algorithm combined with an anti- $k_t$  jet clustering algorithm. The PFlow algorithm [31] utilizes topo-clusters along with information from both the calorimeter systems and the ID in order to make use of the tracker system's advantages in low-energy momentum resolution and angular resolution. First, the energy from charged particles is removed from the calorimeter topo-clusters; then, it is replaced by particle objects created using the remaining energy in the calorimeter and tracks matched to topo-clusters. The ensemble of "particle flow objects" and corresponding matched tracks are used as inputs for the iterative anti- $k_t$  algorithm [32].

The main components of the anti- $k_t$  algorithm involve the distance  $d_{ij}$  between two jet candidates  $i$  and  $j$ , and the distance  $d_{iB}$  between the harder jet candidate of the two (defined as  $i$ ) and the beamline  $B$ . If  $d_{ij} < d_{iB}$ , then the two jet candidates are combined and returned to the pool of candidates; otherwise, jet candidate  $i$  is considered a jet and removed from the pool. The distance  $d_{ij}$  is inversely proportional to a predefined radius parameter  $\Delta R$  in order to control reconstruction quality for small- $R$  and large- $R$  jets. This analysis uses  $\Delta R = 0.4$  to better handle heavily collimated small- $R$  jets resulting from parton

showers.

The anti- $k_t$  jets so far have only been reconstructed at the EM level and need to be calibrated to match the energy scale of jets reconstructed at particle level. This is done via a MC-based jet energy scale (JES) calibration sequence, along with further calibrations to account for pile-up effects and energy leakage. The full JES calibration sequence is shown in Figure 4.2. All calibration except origin correction are applied to the jet’s four-momentum i.e. jet  $p_T$ , energy and mass. Additionally, a jet energy resolution (JER) [33] step is carried out in a similar manner to JES calibration to match the resolution of jets in dijet events.

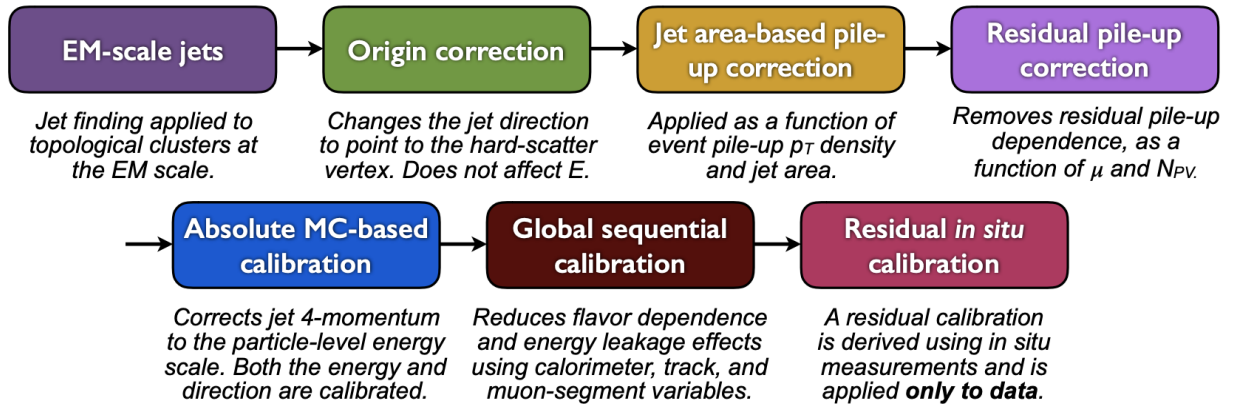


Figure 4.2: Jet energy scale calibration sequence for EM-scale jets [34].

## 4.2.2 Flavor tagging

Identifying and classifying hadronic jets are important tasks for ATLAS physics, for example analyses involving Higgs decays  $H \rightarrow b\bar{b}$  or top quarks. Flavor tagging or  $b$ -tagging is the process of identifying jets containing  $b$ -hadrons,  $c$ -hadrons, light-hadrons ( $uds$ -hadrons) or jets from hadronically decaying  $\tau$  leptons. Distinguishing  $b$ -jets is of particular interest due to their characteristically long lifetime ( $\tau \approx 1.5$  ps), displaced secondary decay vertex and

high decay multiplicity.

Usage of  $b$ -tagging in this analysis is done via five operating points (OPs), corresponding to 65%, 70%, 77%, 85% and 90%  $b$ -jet tagging efficiency  $\varepsilon_b$  in simulated  $t\bar{t}$  events, in order from the loosest to tightest discriminant cut point. The OPs are defined by placing selections on the tagger output to provide a predefined  $\varepsilon_b$  level; the selection cuts act as a variable trade-off between  $b$ -tagging efficiency and  $b$ -jet purity i.e.  $c$ - or light-jet rejection. For this thesis, a jet is considered  $b$ -tagged if it passes the 85% OP. The  $b$ -tagged jet is then assigned a pseudo-continuous  $b$ -tagging (PCBT) score, which quantifies a jet's ability to satisfy different OPs. The score can take integer values between 1 and 6, where a score of 6 is assigned to jets passing all OP thresholds; a score of 2 for jets that pass only the tightest OP (90%); and a score of 1 for jets that pass no OP. A value of -1 is also defined for any jet that does not satisfy  $b$ -tagging criteria.

## **GN2 $b$ -tagging algorithm**

For this analysis,  $b$ -jets are identified and tagged with the GN2v01  $b$ -tagger [35]. The GN2 algorithm uses a Transformer-based model [36] modified to incorporate domain knowledge and additional auxiliary physics objectives: grouping tracks with a common vertex and predicting the underlying physics process for a track. The network structure is shown in Figure 4.3. The GN2  $b$ -tagger forms the input vector by concatenating 2 jet variables and 19 track reconstruction variables (for up to 40 tracks), normalized to zero mean and unit variance. The output consists of a track-pairing output layer of size 2, a track origin classification layer of 7 categories, and a jet classification layer of size 4 for the probability of each jet being a  $b$ -,  $c$ -, light- or  $\tau$ -jet respectively. For  $b$ -tagging purpose, a discriminant is



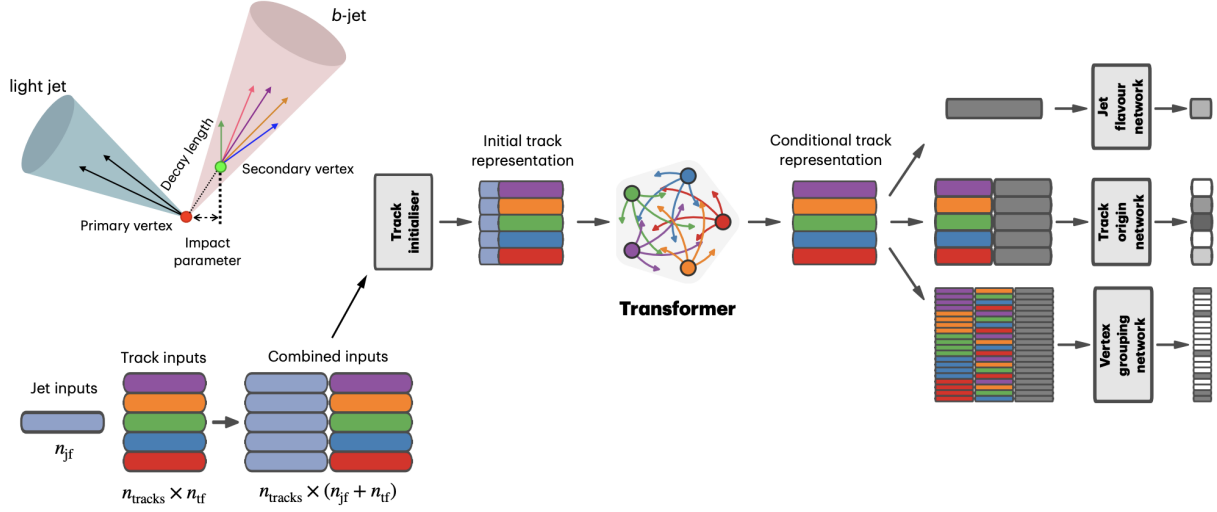


Figure 4.3: Overview of the GN2 architecture. The number of jet and track features are represented by  $n_{\text{jf}}$  and  $n_{\text{tf}}$  respectively. The global jet representation and track embeddings output by the Transformer encoder are used as inputs for three task-specific networks [35].

defined using these four outputs

$$D_b = \ln \left( \frac{p_b}{f_c p_c + f_\tau p_\tau + (1 - f_c - f_\tau) p_{\text{light}}} \right) \quad (4.1)$$

where  $p_x$  is the probability of the jet being an  $x$ -jet as predicted by GN2, and  $f_c$ ,  $f_\tau$  are tunable free parameters controlling balance between  $c$ - and light-jet rejection.

Simulated SM  $t\bar{t}$  and BSM  $Z'$  events from  $pp$  collisions were used as training and evaluation samples. In order to minimize bias, both  $b$ - and light-jet samples are re-sampled to match  $c$ -jet distributions. Figure 4.4 shows the performance of GN2 compared to the previous convolutional neural network-based standard  $b$ -tagging algorithm DL1d, in terms of  $c$ -, light- and  $\tau$ -jet rejection as a function of  $b$ -tagging efficiency. The network gives a factor of 1.5-4 improvement in experimental applications compared to DL1d [35], without dependence on the choice of MC event generator or inputs from low-level flavor tagging algorithm.

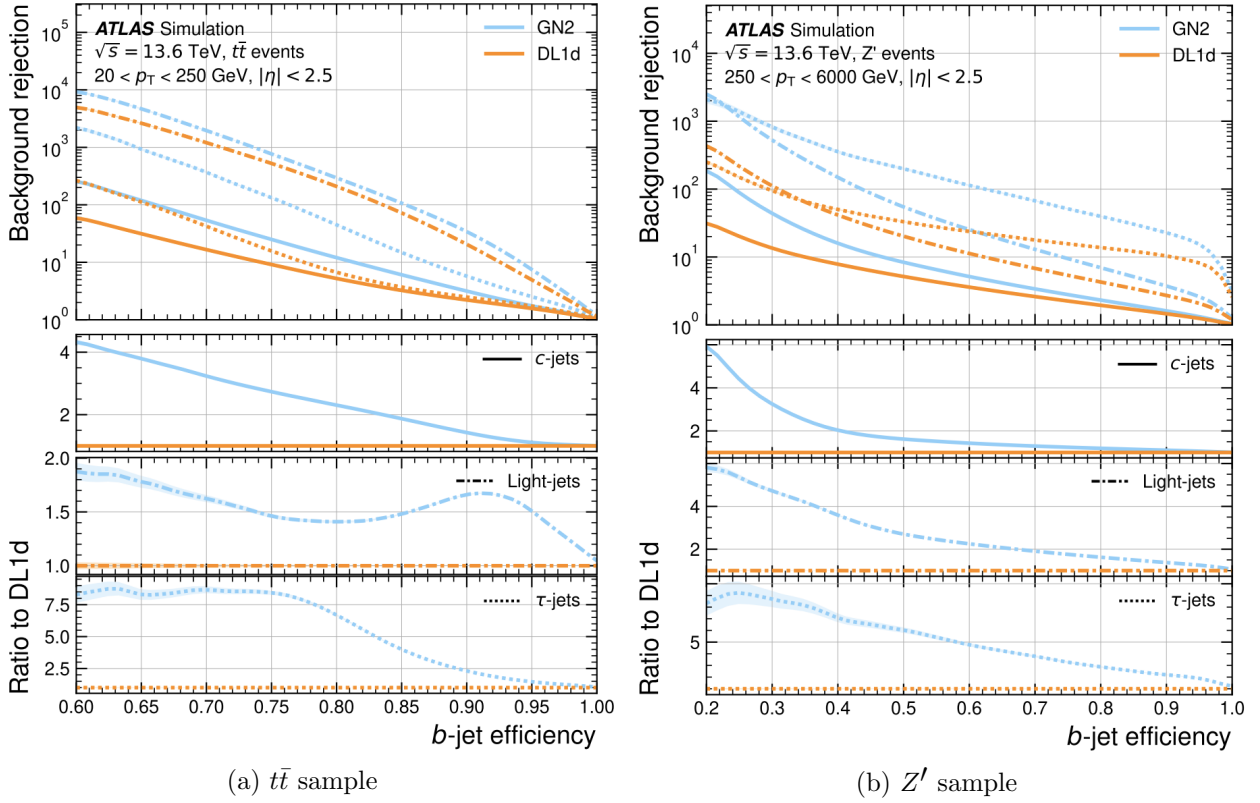


Figure 4.4: The  $c$ -, light- and  $\tau$ -jet rejection rate as a function of  $b$ -tagging efficiency for GN2 and DL1d using (a) jets in the  $t\bar{t}$  sample, and (b) jets in the  $Z'$  sample. The performance ratios of GN2 to DL1d are shown in the bottom panels [35].

## Efficiency calibration

Due to imperfect description of detector response and physics modeling effects in simulation, the  $b$ -tagging efficiency predicted by MC simulation  $\varepsilon_b^{\text{sim}}$  requires a correction factor to match the efficiency measured in collision data  $\varepsilon_b^{\text{data}}$ . The correction scale factors (SF) are defined as  $\text{SF} = \varepsilon_b^{\text{data}} / \varepsilon_b^{\text{sim}}$  and are determined by data-to-MC calibration using samples enriched in dileptonic  $t\bar{t}$  decays [37]. The resulting SFs are applied to MC simulated jets individually.

## 4.3 Leptons

Lepton reconstruction in ATLAS involves electron and muon reconstruction since tau decays quickly, and depending on decay mode can be reconstructed using either jets or light leptons. Leptons can be classified into two categories: prompt leptons resulting from heavy particle decays and non-prompt leptons resulting from detector or reconstruction effects, or from heavy-flavor hadron decays.

### 4.3.1 Electrons

Electrons leave energy signature in the detector by interacting with the detector materials and losing energy in the form of bremsstrahlung photons. A bremsstrahlung photon can produce an electron-positron pair which can itself deposit signals in the detector, creating a cascade of particles that can leave multiple of either tracks in the ID or EM showers in the calorimeters, all of which are considered part of the same EM topo-cluster. Electron signal signature has three characteristic components: localized energy deposits in the calorimeters, multiple tracks in the ID and compatibility between the above tracks and energy clusters in

the  $\eta \times \phi$  plane [19]. Electron reconstruction in ATLAS follows these steps accordingly.

Seed-cluster reconstruction and track reconstruction are performed sequentially in accordance with the iterative topo-clustering algorithm and track reconstruction method described in section 4.1. The seed-cluster and GSF-refitted track candidate not associated with a conversion vertex are matched to form an electron candidate. The cluster energy is then calibrated using multivariate techniques on data and simulation to match the original electron energy.

## Electron identification

Additional LH-based identification selections using ID and EM calorimeter information are implemented to further improve the purity of reconstructed electrons in the central region of the detector ( $|\eta| < 2.47$ ) [19]. The electron LH function is built with the signal being prompt electrons and background being objects with similar signature to prompt electrons i.e. hadronic jet deposits, photon conversions or heavy-flavor hadron decays. Three identification OPs are defined for physics analyses: *Loose*, *Medium* and *Tight*, optimized for 9 bins in  $|\eta|$  and 12 bins in  $E_T$  with each OP corresponding to a fixed efficiency requirement for each bin. For typical EW processes, the target efficiencies for *Loose*, *Medium* and *Tight* start at 93%, 88% and 80% respectively and increase with  $E_T$ . Similar to  $b$ -tagging OPs, the electron identification OPs represent a trade-off in signal efficiency and background rejection. The electron efficiency are estimated using tag-and-probe method on samples of  $J/\Psi \rightarrow ee$  and  $Z \rightarrow ee$  [19].

## Electron isolation

A characteristic distinction between prompt electrons and electrons from background processes is the relative lack of activity in both the ID and calorimeters within an  $\Delta\eta \times \Delta\phi$  area surrounding the reconstruction candidate. Calorimeter-based and track-based electron isolation variables [19] are defined to quantify the amount of activity around the electron candidate using topo-clusters and reconstructed tracks respectively.

Calorimeter-based isolation variables  $E_{\text{T}}^{\text{cone}XX}$  are computed by first summing the energy of topo-clusters with barycenters falling within a cone of radius  $\Delta R = \sqrt{(\Delta\eta)^2 + (\Delta\phi)^2} = XX/100$  around the direction of the electron candidate. The final isolation variables are obtained by subtracting from the sum the energy belonging to the candidate electron at the core of the cone, then applying corrections for pile-up effects and energy leakage outside of the core. Similar to calorimeter-based variables, track-based isolation variables  $p_{\text{T}}^{\text{varcone}XX}$  are calculated by summing all track  $p_{\text{T}}$  within a cone of radius  $\Delta R$  around the electron candidate, minus the candidate's contribution. The cone radius is variable as a function of  $p_{\text{T}}$  and is described as

$$\Delta R \equiv \min\left(\frac{10}{p_{\text{T}}}, \Delta R_{\text{max}}\right), \quad (4.2)$$

where  $p_{\text{T}}$  is expressed in GeV and  $\Delta R_{\text{max}}$  is the maximum cone size, defined to account for closer proximity of decay products to the electron in high-momentum heavy particle decays. Four isolation operating points are implemented to satisfy specific needs by physics analyses: *Loose*, *Tight*, *HighPtCaloOnly* and *Gradient* [19].

## Electron charge misidentification

Charge misidentification is a crucial irreducible background, particularly for analyses with electron charge selection criteria. Electron charge is determined by the curvature of the associated reconstructed track, and misidentification of charge can occur via either an incorrect curvature measurement or an incorrectly matched track. Inaccurate measurement is more likely for high energy electrons due to the small curvature in track trajectories at high  $p_T$ , while track matching error usually results from bremsstrahlung pair-production generating secondary tracks in close proximity [19]. Suppression of this background is assisted via a boosted decision tree discriminant named the Electron Charge ID Selector (ECIDS) [39]. The addition of ECIDS removed 90% of electrons with incorrect charge while selecting 98% of electrons with correct charge from electrons in  $Z \rightarrow ee$  events satisfying *Medium*/*Tight* identification and *Tight* isolation criteria.

### 4.3.2 Muons

Muons act as minimum-ionizing particles, leaving tracks in the MS or characteristics energy deposits in the calorimeter and can be reconstructed globally using information from the ID, MS and calorimeters. Five reconstruction strategies corresponding to five muon types [40] are utilized in ATLAS:

- Combined (CB): the primary ATLAS muon reconstruction method. Combined muons are first reconstructed using MS tracks then extrapolated to include ID tracks (outside-in strategy). A global combined track fit is performed on both MS and ID tracks.
- Inside-out combined (IO): complementary to CB reconstruction. IO muon tracks are extrapolated from ID to MS, then fitted with MS hits and calorimeter energy loss in a

combined track fit.

- MS extrapolated (ME): ME muons are defined as muons with a MS track that cannot be matched to an ID track using CB reconstruction. ME muons allow extension of muon reconstruction acceptance to regions not covered by the ID ( $2.5 < |\eta| < 2.7$ )
- Segment-tagged (ST): ST muons are defined as a successfully matched ID track that satisfies tight angular matching criteria to at least one reconstructed MDT or CSC segment when extrapolated to the MS. MS reconstruction is used primarily when muons only crossed one layer of MS chambers.
- Calorimeter-tagged (CT): CT muons are defined as an ID track that can be matched to energy deposits consistent with those of a minimum-ionizing particle when extrapolated through the calorimeter. CT reconstruction extends acceptance range to regions in the MS with sparse instrumentation ( $|\eta| < 0.1$ ) with a higher  $p_T$  threshold of 5 GeV, compared to the 2 GeV threshold used by other muon reconstruction algorithms due to large background contamination at the low  $p_T$  range of  $15 < p_T < 100$  GeV [41].

## Muon identification

Reconstructed muons are further filtered by identification criteria to select for high-quality prompt muons. Requirements include number of hits in the MS and ID, track fit properties and compatibility between measurements of the two systems. Three standard OPs (*Loose*, *Medium*, *Tight*) are defined to better match the needs of different physics analyses concerning prompt muon  $p_T$  resolution, identification efficiency and non-prompt muon rejection. The default identification OP for ATLAS physics is *Medium* which provides efficiency and purity suitable for a wide range of analyses while minimizing systematic uncertainties [40].

## Muon isolation

Muons from heavy particle decays are often produced in an isolated manner compared to muons from semileptonic decays, and is therefore an important tool for background rejection in many physics analyses. Muon isolation strategies are similar to that of electron in subsection 4.3.1, with track-based and calorimeter-based isolation variables. Seven isolation OPs are defined using either or both types of isolation variables [40].

## 4.4 Missing transverse momentum

Collisions at the LHC happen along the  $z$ -axis of the ATLAS coordination system between two particle beam of equal center-of-mass energy. By conservation of momentum, the sum of transverse momenta of outgoing particles should be zero. A discrepancy between measured momentum and zero would then suggest the presence of undetectable particles, which would consist of either SM neutrinos or some unknown BSM particles, making missing transverse momentum ( $E_T^{\text{miss}}$ ) an important observable to reconstruct.

Reconstructing  $E_T^{\text{miss}}$  utilizes information from fully reconstructed leptons, photons, jets and other matched track-vertex objects not associated with a prompt object (soft signals), defined with respect to the  $x(y)$ -axis as

$$E_{x(y)}^{\text{miss}} = - \sum_{i \in \{\text{hard objects}\}} p_{x(y),i} - \sum_{j \in \{\text{soft signals}\}} p_{x(y),j}, \quad (4.3)$$



939 where  $p_{x(y)}$  is the  $x(y)$ -component of  $p_T$  for each particle [42]. The following observables  
 940 can then be defined:

$$\begin{aligned}
 \mathbf{E}_T^{\text{miss}} &= (E_x^{\text{miss}}, E_y^{\text{miss}}), \\
 E_T^{\text{miss}} &= |\mathbf{E}_T^{\text{miss}}| = \sqrt{(E_x^{\text{miss}})^2 + (E_y^{\text{miss}})^2}, \\
 \phi^{\text{miss}} &= \tan^{-1}(E_y^{\text{miss}}/E_x^{\text{miss}}),
 \end{aligned} \tag{4.4}$$

941 where  $E_T^{\text{miss}}$  represents the magnitude of the missing transverse energy vector  $\mathbf{E}_T^{\text{miss}}$ , and  
 942  $\phi^{\text{miss}}$  its direction in the transverse plane. The vectorial sum  $\mathbf{E}_T^{\text{miss}}$  can be broken down into

$$\mathbf{E}_T^{\text{miss}} = - \underbrace{\sum_{\text{selected electrons}} \mathbf{p}_T^e - \sum_{\text{selected muons}} \mathbf{p}_T^\mu - \sum_{\text{accepted photons}} \mathbf{p}_T^\gamma - \sum_{\text{accepted } \tau\text{-leptons}} \mathbf{p}_T^\tau - \sum_{\text{accepted jets}} \mathbf{p}_T^{\text{jet}}}_{\text{hard term}} - \underbrace{\sum_{\text{unused tracks}} \mathbf{p}_T^{\text{track}}}_{\text{soft term}}. \tag{4.5}$$

943 Two OPs are defined for  $E_T^{\text{miss}}$ , *Loose* and *Tight*, with selections on jet  $p_T$  and JVT criteria  
 944 [43]. The *Tight* OP is used in this analysis; *Tight* reduces pile-up dependence of  $E_T^{\text{miss}}$   
 945 by removing the phase space region containing more pile-up than hard-scatter jets, at the  
 946 expense of resolution and scale at low pile-up,

## 947 4.5 Overlap removal

948 Since different objects are reconstructed independently, it is possible for the same detector  
 949 signals to be used to reconstruct multiple objects. An overlap removal strategy is imple-  
 950 mented to resolve ambiguities; the overlap removal process for this analysis applies selections  
 951 in Table 4.1 sequentially, from top to bottom.

Table 4.1: Overlap removal process for this analysis, applied sequentially from top to bottom.

Remove	Keep	Matching criteria
Electron	Electron	Shared ID track, $p_{T,1}^e < p_{T,2}^e$
Muon	Electron	Shared ID track, CT muon
Electron	Muon	Shared ID track
Jet	Electron	$\Delta R < 0.2$
Electron	Jet	$\Delta R < 0.4$
Jet	Muon	$(\Delta R < 0.2 \text{ or ghost-associated}) \ \& \ N_{\text{track}} < 3$
Muon	Jet	$\Delta R < \min(0.4, 0.04 + 10\text{GeV}/p_T^\mu)$

## 4.6 Object definition

Table 4.2 shows the selections used in this analysis. Each selection comes with associated calibration scale factors to account for discrepancies between data and MC simulation, and are applied multiplicatively to MC event weights.

Table 4.2: Summary of object selection criteria used in this analysis .

Selection	Electrons	Muons	Jets
$p_T$ [GeV]	$> 15$ $p_T(l_0) > 28$	$> 15$	$> 20$
$ \eta $	$1.52 \leq  \eta  < 2.47$ $< 1.37$	$< 2.5$	$< 2.5$
Identification	<i>TightLH</i> pass ECIDS ( $ee/e\mu$ )	<i>Medium</i>	NNJvt <i>FixedEffPt</i> ( $p_T < 60,  \eta  < 2.4$ )
Isolation	<i>Tight_VarRad</i>	<i>PflowTight_VarRad</i>	
Track-vertex assoc.			
$ d_0^{\text{BL}}(\sigma) $	$< 5$	$< 3$	
$ \Delta z_0^{\text{BL}} \sin \theta $ [mm]	$< 0.5$	$< 0.5$	

# Chapter 5. Data & Simulated Samples

## 5.1 Data samples

LHC Run 2 data collected at  $\sqrt{s} = 13$  TeV between 2015-2018

luminosity  $140 \text{ fb}^{-1}$

(include uncertainty for Run 2 only)

Triggers used:

Table 5.1: Caption

Trigger	Data period			
	2015	2016	2017	2018
Single electron triggers				
HLT_e24_lhmedium_L1EM20VH	✓	-	-	-
HLT_e60_lhmedium	✓	-	-	-
HLT_e120_lhloose	✓	-	-	-
HLT_e26_lhtight_nod0_ivarloose	-	✓	✓	✓
HLT_e60_lhmedium_nod0	-	✓	✓	✓
HLT_e140_lhloose_nod0	-	✓	✓	✓
Di-electron triggers				
HLT_2e12_lhloose_L12EM10VH	✓	-	-	-
HLT_2e17_lhvloose_nod0	-	✓	-	-
HLT_2e24_lhvloose_nod0	-	-	✓	✓
HLT_2e17_lhvloose_nod0_L12EM15VHI	-	-	-	✓
Single muon trigger				
HLT_mu20_iloose_L1MU15	✓	-	-	-
HLT_mu40	✓	-	-	-
HLT_mu26_ivarmedium	-	✓	✓	✓
HLT_mu50	-	✓	✓	✓

## 5.2 Monte Carlo samples

Monte Carlo simulated samples are used to estimate signal acceptance before unblinding, profile the physics background for the analysis and to study object optimizations. Simulated samples for this analysis use are generated from ATLAS' generalized MC20a/d/e samples for Run 2, using full detector simulation (FS) and fast simulation (AF3) to simulate detector response.

### 5.2.1 $t\bar{t}Z'$ signal samples

Signal  $t\bar{t}Z'$  samples were generated based on the simplified top-philic resonance model in subsection 2.2.1 where a color singlet vector resonance couples strongly to only top and antitop. Six  $Z'$  mass points were utilized for the generation of the signal sample: 1000, 1250, 1500, 2000, 2500 and 3000 GeV. From subsection 2.2.1, the top- $Z'$  coupling  $c_t$  is chosen to be 1 for a narrow resonance peak, and the chirality angle  $\theta$  is chosen to be  $\pi/4$  to suppress loop production of  $Z'$ . The samples were then generated with MADGRAPH5\_AMC@NLO v.3.5.0 [45] at LO with the NNPDF3.1L0 [46] PDF set interfaced with PYTHIA8 [47] using A14 tune and NNPDF2.31o PDF set for parton showering and hadronization. The resonance width is calculated to be 4% for  $c_t = 1$ .

plots:  $H_T$ , nJets, parameter comparison, interference,  $m_{t\bar{t}}$  invariant mass

Table 5.2: Summary of all Monte-Carlo samples used in this analysis.

Process	ME Generator	ME Order	ME PDF	PS	Tune	Sim.
<b>Signals</b>						
$t\bar{t}Z'$	MADGRAPH5_AMC@NLO	LO	NNPDF3.1LO	PYTHIA8	A14	FS
$t\bar{t}t\bar{t}$ and $t\bar{t}t$						
$t\bar{t}t\bar{t}$	MADGRAPH5_AMC@NLO	NLO	NNPDF3.0nlo	PYTHIA8	A14	AF3
	MADGRAPH5_AMC@NLO	NLO	MMHT2014 LO	HERWIG7 H7-UE- MMHT		AF3
	SHERPA	NLO	NNPDF3.0nnlo	HERWIG7	SHERPA	FS
$t\bar{t}t$	MADGRAPH5_AMC@NLO	LO	NNPDF2.3lo	PYTHIA8	A14	AF3
$t\bar{t}V$						
$t\bar{t}H$	POWHEGBOX v2	NLO	NNPDF3.0nlo	PYTHIA8	A14	FS
	POWHEGBOX v2	NLO	NNPDF3.0nlo	HERWIG7 H7.2- Default		FS
$t\bar{t}(Z/\gamma^*)$	MADGRAPH5_AMC@NLO	NLO	NNPDF3.0nlo	PYTHIA8	A14	FS
	SHERPA	NLO	NNPDF3.0nnlo	SHERPA	SHERPA	FS
$t\bar{t}W$	SHERPA	NLO	NNPDF3.0nnlo	SHERPA	SHERPA	FS
	SHERPA	LO	NNPDF3.0nnlo	SHERPA	SHERPA	FS
$t\bar{t}$ and Single-Top						
$t\bar{t}$	POWHEGBOX v2	NLO	NNPDF3.0nlo	PYTHIA8	A14	FS
$tW$	POWHEGBOX v2	NLO	NNPDF3.0nlo	PYTHIA8	A14	FS
$t(q)b$	POWHEGBOX v2	NLO	NNPDF3.0nlo (s) NNPDF3.0nlo 4f (t)	PYTHIA8	A14	FS FS
$tWZ$	MADGRAPH5_AMC@NLO	NLO	NNPDF3.0nlo	PYTHIA8	A14	FS
$tZ$	MADGRAPH5_AMC@NLO	LO	NNPDF3.0nlo 4f	PYTHIA8	A14	FS
$t\bar{t}VV$						
$t\bar{t}WW$	MADGRAPH5_AMC@NLO	LO	NNPDF3.0nlo	PYTHIA8	A14	FS
$t\bar{t}WZ$	MADGRAPH	LO	NNPDF3.0nlo	PYTHIA8	A14	AF3
$t\bar{t}HH$	MADGRAPH	LO	NNPDF3.0nlo	PYTHIA8	A14	AF3
$t\bar{t}WH$	MADGRAPH	LO	NNPDF3.0nlo	PYTHIA8	A14	AF3
$t\bar{t}ZZ$	MADGRAPH	LO	NNPDF3.0nlo	PYTHIA8	A14	AF3
$V(VV)+\text{jets}$ and $VH$						
$V+\text{jets}$	SHERPA	NLO	NNPDF3.0nnlo	SHERPA	SHERPA	FS
$VV+\text{jets}$	SHERPA	NLO	NNPDF3.0nnlo	SHERPA	SHERPA	FS
		LO ( $gg \rightarrow VV$ )				FS
$VVV+\text{jets}$	SHERPA	NLO	NNPDF3.0nnlo	SHERPA	SHERPA	FS
$VH$	POWHEGBOX v2	NLO	NNPDF3.0aznlo	PYTHIA8	A14	FS

## 5.2.2 Background samples

### SM $t\bar{t}t\bar{t}$ background

Nominal SM  $t\bar{t}t\bar{t}$  sample was generated with MADGRAPH5\_AMC@NLO [45] at NLO in QCD with the NNPDF3.0nlo [46] PDF set and interfaced with PYTHIA8.230 [47] using A14 tune [48]. Decays for top quarks are simulated LO with MADSPIN [49, 50] to preserve spin information, while decays for  $b$ - and  $c$ -hadrons are simulated with EVTGEN v1.6.0 [51]. The renormalization and factorization scales  $\mu_R$  and  $\mu_F$  are set to  $\sqrt{m^2 + p_T^2}/4$ , which represents the sum of transverse mass of all particles generated from the ME calculation [52]. The ATLAS detector response was simulated with AF3. Additional auxiliary  $t\bar{t}t\bar{t}$  samples are also generated to evaluate the impact of generator and PS uncertainties as shown in 5.2.

### $t\bar{t}W$ background

Nominal  $t\bar{t}W$  sample was generated using SHERPA v2.2.10 [53] at NLO in QCD with the NNPDF3.0nnlo [46] PDF with up to one extra parton at NLO and two at LO, which are matched and merged with SHERPA PS based on Catani-Seymour dipole factorization [54] using the MEPS@NLO prescription [55–58] and a merging scale of 30 GeV. Higher-order ME corrections are provided in QCD by the OpenLoops 2 library [59–61] and in EW from  $\mathcal{O}(\alpha^3) + \mathcal{O}(\alpha_S^2\alpha^2)$  (LO3 & NLO2) via two sets of internal event weights. An alternative sample with only EW corrections at LO from  $\mathcal{O}(\alpha_S\alpha^3)$  (NLO3) diagrams were also simulated with the same settings.

## 998 $t\bar{t}(Z/\gamma^*)$ background

999 Nominal  $t\bar{t}(Z/\gamma^*)$  samples were generated separately for different ranges of dilepton in-  
1000 variant mass  $m_{\ell\ell}$  to account for on-shell and off-shell  $Z/\gamma^*$  production. Sample for  $m_{\ell\ell}$   
1001 between 1 and 5 GeV was produced using MADGRAPH5\_AMC@NLO [45] at NLO with  
1002 the NNPDF3.0nnlo [46] PDF set, interfaced with PYTHIA8.230 [47] using A14 tune [48] and  
1003 NNPDF2.31o PDF set. Sample for  $m_{\ell\ell} < 5$  GeV was produced with SHERPA v2.2.10 [53]  
1004 at NLO using NNPDF3.0nnlo PDF set. To account for generator uncertainty, an alternative  
1005  $m_{\ell\ell} > 5$  GeV sample was generated with identical settings to the low  $m_{\ell\ell}$  sample. The  
1006 ATLAS detector response was simulated with full detector simulation (FS).

# Chapter 6. Analysis Strategy

## 6.1 Event selection

Events for the analysis first are preselected following a list of criteria to optimize for event quality and background rejection.

The criteria are applied sequentially from top to bottom along with cleaning and veto cuts

1. **Good Run List (GRL)**: data events must be part of a predefined list of suitable runs and luminosity blocks.

2. **Primary vertex**: events must have at least one reconstructed vertex matched to 2 or more associated tracks with  $p_T > 500$  MeV.

3. **Trigger**: events must be selected by at least one trigger documented in ??.

4. **Kinematic selection**: events must have exactly two Tight leptons with the same electric charge, or at lease three Tight leptons of any charge. The leading lepton must have  $p_T > 28$  GeV, and all leptons must satisfy  $p_T > 15$  GeV.

Events are separated into two channels based on the number of leptons: same-sign di-lepton (SS2L) for events with exactly two leptons of the same charge, or multilepton (ML) for events with three or more leptons. The channels are further separated into regions defined in section 6.2 to prepare for analysis.

Further selections are applied based on the lepton flavors present. In the SS2L channel, if both leptons are electrons, the invariant mass  $m_{ll}$  must satisfy  $m_{ll} < 81$  GeV and  $m_{ll} > 101$  GeV to suppress background involving  $Z$ -bosons. In the ML channel, the same criteria must be satisfied for every opposite-sign same-flavor pair of leptons in an event.



## Event categorization

Simulated events are categorized using truth information of leptons ( $e/\mu$ ) and their originating MC particle (mother-particle).

Each lepton can be classified as either prompt or non-prompt, with non-prompt leptons further categorized for background estimation purposes.

If an event contains only prompt leptons, the event is classified as its corresponding process.

If the event contains one non-prompt lepton, the event is classified as the corresponding type of the non-prompt lepton. If the event contains more than one non-prompt lepton, the event is classified as other.

- **Prompt:** if the lepton originates from  $W/Z/H$  boson decays, or from a mother-particle created by a final state photon.

- **Non-prompt:**

- **Charge-flip ( $e$  only):** if the reconstructed charge of the lepton differs from that of the first mother-particle.

- **Material conversion ( $e$  only):** if the lepton originated from a photon conversion and the mother-particle is an isolated prompt photon, non-isolated final state photon, or heavy boson.

- **$\gamma$ -conversion ( $e$  only):** if the lepton originated from a photon conversion and the mother-particle is a background electron.

- **Heavy flavor decay:** if the lepton originated from a  $b$ - or  $c$ -hadron.

- **Fake:** if the lepton originated from a light- or  $s$ -hadron, or if the truth type of the lepton is hadron.

– **Other**: any lepton that does not belong to one of the above categories.

## 6.2 Analysis regions

Events are selected and categorized into analysis regions belonging to one of two types: control regions (CRs) enriched in background events, and signal regions (SRs) enriched in signal events. This allows for the examination and control of backgrounds and systematic uncertainties, as well as study of signal sensitivities.

The signal is then extracted from the SRs with a profile LH fit using all regions. The full selection criteria for each region are summarized in Table 6.3

### 6.2.1 Signal regions

- All events selected for SS2L and 3L signal regions must satisfy the following criteria:

- Contains 6 or more jets, with at least 2 jets  $b$ -tagged at the 85% WP
- Scalar sum of the transverse momenta of all leptons and jets  $H_T > 500$  GeV
- Dilepton invariant mass  $m_{\ell\ell}$  does not coincide with the  $Z$ -boson mass range of 81 – 101 GeV

- The SR is further granularized by the number of  $b$ -jets and leptons to further study and improve signal sensitivity

Table 6.1: Caption

SR	Selection criteria	
	$b$ -jets	leptons
2b2l	$N_b = 2$	$N_l = 2$
2b3l4l	$N_b = 2$	$N_l \geq 3$
3b2l	$N_b = 3$	$N_l = 2$
3b3l4l	$N_b = 3$	$N_l \geq 3$
4b	$N_b = 4$	

### 6.2.2 Control regions

Control regions are defined for each background to be enriched in the targeted background events, in order to maximize the targeted background's purity and minimize contamination from other sources within the region.

This helps to constrain and reduce correlation between background normalization factors.

Fit variables and selection criteria are determined via optimization studies on CRs to achieve the largest discriminating power possible between the target background and other event types.

#### $t\bar{t}W$ background CRs

Two types of CRs are defined to estimate the flavor composition and normalization of  $t\bar{t}W$  +jets background: CR  $t\bar{t}W^\pm$ +jets to constrain flavor composition, and CR 1b( $\pm$ ) to constrain jet multiplicity spectrum.

These are further split into CR  $t\bar{t}W^\pm$  and CR 1b( $\pm$ ) due to the pronounced asymmetry in  $t\bar{t}W$  production from  $pp$  collisions, with  $t\bar{t}W^+$  being produced at approximately twice the rate of  $t\bar{t}W^-$ . Selections on  $H_T$  and  $N_{\text{jets}}$  to ensure orthogonality to SR

Selections on total charge for each charged  $W^\pm$  boson

1083

1084 **Fake/non-prompt background CRs**

1085 Selection for fake/non-prompt CRs are determined using the `DFCommonAddAmbiguity` (DF-  
1086 CAA) variable for reconstructed leptons.

Table 6.2: Caption

DFCAA	Description
-1	No 2nd track found
0	2nd track found, no conversion found
1	Virtual photon conversion candidate
2	Material conversion candidate

1087 Four CRs for three main types of fake/non-prompt backgrounds: virtual photon ( $\gamma^*$ )  
1088 conversion, photon conversion in detector material (Mat. Conv.) and heavy flavor decays  
1089 (HF).

1090

- 1091 • Low  $m_\gamma^*$ : events with an  $e^+e^-$  pair produced from a virtual photon  
1092 Selects two same-sign leptons with at least one electron reconstructed as an internal  
1093 conversion candidate and neither as with a material conversion candidate ( $\text{DFCAA}_{\ell_1(\ell_2)} =$   
1094 1 and  $\neq 2$ )  
1095 NF constrained using yield count only.
- 1096 • Mat. Conv.: events with an electron originating from photon conversion within the  
1097 detector material.  
1098 Selects two same-sign leptons with at least one electron reconstructed as a material  
1099 conversion candidate ( $\text{DFCAA}_{\ell_1(\ell_2)} = 2$ ).

NF constrained using yield count only.

- HF  $e/\mu$ : events with a reconstructed non-prompt lepton from semi-leptonic decays of  $b$ - and  $c$ -hadrons (heavy flavor decays)

Selects three leptons with at least two electrons/muons, with no lepton reconstructed as a conversion candidate (DFCAA < 0).

NFs constrained by fitting with  $p_T$  of the third leading lepton  $\ell_3$ .

### 6.2.3 Validation regions

In addition, validation regions are also defined to validate the normalization and modeling of  $t\bar{t}Z$  and  $t\bar{t}W$  background without being used in the fit.

- $t\bar{t}Z$ : Selects events with at least two  $b$ -tagged jets, at least four total jets and three leptons with at least one same-flavor opposite-sign lepton pair possessing invariant mass  $m_{\ell\ell}$  within the  $Z$ -boson mass window of  $81 - 101$  GeV

- $t\bar{t}W$ : Main charge asymmetric background leaning  $t\bar{t}W^+$ , validated using the difference in number of positively and negatively charged events  $N_+ - N_-$  instead of total number of events.

Selects using CR  $t\bar{t}W$  and CR 1b criteria, with one VR not orthogonal to SR and one orthogonal VR with more limited statistics.

## 6.3 Background estimation

Background events in this analysis consist of SM processes that can result in a  $t\bar{t}t\bar{t}$  SSML final state.

Table 6.3: Caption

Region	Channel	$N_{\text{jets}}$	$N_b$	Other selections	Fitted variable
CR Low $m_{\gamma^*}$	SS $e\ell$	[4, 6)	$\geq 1$	$\ell_1/\ell_2$ is from virtual photon decay $\ell_1 + \ell_2$ not from material conversion	event yield
CR Mat. Conv.	SS $e\ell$	[4, 6)	$\geq 1$	$\ell_1/\ell_2$ is from material conversion	event yield
CR HF $\mu$	$\ell\mu\mu$	$\geq 1$	1	$\ell_1 + \ell_2$ not conversion candidates $100 < H_T < 300$ GeV $E_T^{\text{miss}} > 35$ GeV total charge = $\pm 1$	$p_T(\ell_3)$
CR HF $e$	$e\ell\ell$	$\geq 1$	1	$\ell_1 + \ell_2$ not conversion candidates $100 < H_T < 275$ GeV $E_T^{\text{miss}} > 35$ GeV total charge = $\pm 1$	$p_T(\ell_3)$
CR $t\bar{t}W^+$	SS $\ell\mu$	$\geq 4$	$\geq 2$	$ \eta(e)  < 1.5$ for $N_b = 2$ : $H_T < 500$ GeV or $N_{\text{jets}} < 6$ for $N_b \geq 3$ : $H_T < 500$ GeV total charge $> 0$	$N_{\text{jets}}$
CR $t\bar{t}W^-$	SS $\ell\mu$	$\geq 4$	$\geq 2$	$ \eta(e)  < 1.5$ for $N_b = 2$ : $H_T < 500$ GeV or $N_{\text{jets}} < 6$ for $N_b \geq 3$ : $H_T < 500$ GeV total charge $< 0$	$N_{\text{jets}}$
CR 1b(+)	SS2L+3L	$\geq 4$	1	$\ell_1 + \ell_2$ not from material conversion $H_T > 500$ GeV total charge $> 0$	$N_{\text{jets}}$
CR 1b(-)	SS2L+3L	$\geq 4$	1	$\ell_1 + \ell_2$ not from material conversion $H_T > 500$ GeV total charge $< 0$	$N_{\text{jets}}$
VR $t\bar{t}Z$	3L $\ell^\pm\ell^\mp$	$\geq 4$	$\geq 2$	$m_{\ell\ell} \in [81, 101]$ GeV	$N_{\text{jets}}, m_{\ell\ell}$
VR $t\bar{t}W + 1b$	SS2L+3L			CR $t\bar{t}W^\pm$    CR 1b( $\pm$ )	$N_{\text{jets}}$
VR $t\bar{t}W + 1b + \text{SR}$	SS2L+3L			CR $t\bar{t}W^\pm$    CR 1b( $\pm$ )    SR	$N_{\text{jets}}$
SR	SS2L+3L	$\geq 6$	$\geq 2$	$H_T > 500$ GeV $m_{\ell\ell} \notin [81, 101]$ GeV	$H_T$

1120 Can be divided into two types: reducible and irreducible.  
 1121 Reducible background consists of processes that do not result in SSML final state physically,  
 1122 but are reconstructed as such due to erroneous detector and reconstruction effects.  
 1123 Three main types: charge misidentification (QmisID), fake leptons and non-prompt leptons.  
 1124 Estimated using template fitting method to adjust MC predictions via floating normalization  
 1125 factors constrained in the CRs.  
 1126 Irreducible background consists of SM processes that result in SSML final states physically,  
 1127 with all leptons being prompt.  
 1128 Main irreducible background considered in this analysis:  $t\bar{t}\bar{\ell}$ ,  $t\bar{t}W$ ,  $t\bar{t}Z$ , and  $t\bar{t}H$  with smaller  
 1129 contributions from  $VV$ ,  $VVV$ ,  $VH$  and rarer processes like  $t\bar{t}VV$ ,  $tWZ$ ,  $tZq$  and  $t\bar{t}t$ .  
 1130 Most irreducible backgrounds are estimated using MC simulations normalized to their the-  
 1131 oretical SM cross sections (template fitting), with the exception of  $t\bar{t}W$  background due to  
 1132 MC mismodeling of the process at high jet multiplicities.  
 1133 The  $t\bar{t}W$  is instead given four dedicated CRs, and estimated using a data-driven method  
 1134 with a fitted function parameterized in  $N_{\text{jets}}$   
 1135 All CRs and SR are included in the final LH-fit to data.

### 1136 **6.3.1 Template fitting for fake/non-prompt estimation**

1137 Template fit method is a semi-data-driven approach that estimates fake/non-prompt back-  
 1138 ground distributions by fitting the MC kinematic profiles of background processes arising  
 1139 from fake/non-prompt leptons to data.  
 1140 Each of the four main sources of fake/non-prompt leptons is assigned a free-floating normal-  
 1141 ization factor constrained by a CR enriched with the corresponding background. The NFs  
 1142 are determined simultaneously with the signal.

- $NF_{HF\ e(\mu)}$ : events with one reconstructed non-prompt electron (muon) from heavy flavor decays,
- $NF_{Mat.\ Conv.}$ : events with one reconstructed non-prompt electrons from photon conversion in the detector material
- $NF_{Low\ m_{\gamma^*}}$ : events with one reconstructed non-prompt electrons in an  $e^+e^-$  pair from virtual photon ( $\gamma^*$ ) conversion.

### 6.3.2 Charge misidentification data-driven estimation

The same-sign di-lepton channel in the analysis gives rise to a major background contamination in opposite-sign di-lepton events with one misidentified charge.

Charge misidentification occurs via incorrect track curvature measurements or trident electron contamination from bremsstrahlung, and therefore mainly concerns electrons due to muons' low bremsstrahlung rate and precise curvature information using the ID and MS.

The charge misidentification rates is significant at higher  $p_T$  and varies with  $|\eta|$  as a proxy for the amount of detector material the electron interacted with, and is consequently estimated in this analysis using a data-driven method with assistance from ECIDS.

The charge flip probability  $\epsilon$  is estimated using a sample of  $Z \rightarrow e^+e^-$  events with additional constraints on the invariant mass  $m_{ee}$  to be within 10 GeV of the  $Z$ -boson mass.

The  $Z$ -boson mass window is defined to be within  $4\sigma$  to include most events within the peak, and is determined by fitting the  $m_{ee}$  spectrum of the two leading electrons to a Breit-Wigner function, resulting in a range of  $[65.57, 113.49]$  for SS events and  $[71.81, 109.89]$  for OS events.

Background contamination near the peak is assumed to be uniform and subtracted using a sideband method.



1165 Since the  $Z$ -boson decay products consist of a pair of opposite-sign electrons, all same-sign  
 1166 electron pairs are considered to be affected by charge misidentification.  
 1167 Assuming the charge flip probabilities of electrons in an event are uncorrelated, the number  
 1168 of events with same-sign electrons  $N_{ij}^{\text{SS}}$  with the leading electron in the  $i^{\text{th}}$  2D bin in  $(p_{\text{T}}, |\eta|)$   
 1169 and the sub-leading electron in the  $j^{\text{th}}$  bin can be estimated as

$$N_{ij}^{\text{SS}} = N_{ij}^{\text{tot}}(\epsilon_i(1 - \epsilon_j) + \epsilon_j(1 - \epsilon_i)), \quad (6.1)$$

where  $N_{ij}^{\text{tot}}$  is the total number of events in the  $i^{\text{th}}$  and  $j^{\text{th}}$  bin regardless of charge, and  $\epsilon_{i(j)}$  is the charge flip rate in the  $i^{\text{th}}(j^{\text{th}})$  bin.

Assuming  $N_{ij}^{\text{SS}}$  follows a Poisson distribution around the expectation value  $\bar{N}_{ij}^{\text{SS}}$ , the charge flip rate  $\epsilon$  can be estimated by minimizing a negative-LLH function parameterized in  $p_{\text{T}}$  and  $|\eta|$ ,

$$-\ln(\mathcal{L}(\epsilon|N_{\text{SS}})) = -\ln \prod_{ij} \frac{(N_{ij}^{\text{tot}})^{N_{ij}^{\text{SS}}} \cdot e^{-N_{ij}^{\text{tot}}}}{N_{ij}^{\text{SS}}!} \quad (6.2)$$

$$= -\sum_{ij} \left[ N_{ij}^{\text{SS}} \ln(N_{ij}^{\text{tot}}(\epsilon_i(1 - \epsilon_j) + \epsilon_j(1 - \epsilon_i))) - N_{ij}^{\text{tot}}(\epsilon_i(1 - \epsilon_j) + \epsilon_j(1 - \epsilon_i)) \right].$$

$$(6.3)$$

1170 The charge flip rate is then calculated separately for SR and CRs with different electron  
 1171 definitions (CR Low  $m_{\gamma^*}$ , CR Mat. Conv., CR  $t\bar{t}W$ ) using events satisfying 2LSS kinematic  
 1172 selections but with OS electrons, after applying region-specific lepton selections and ECIDS.  
 1173 The following weight is applied to OS events to correct for misidentified SS events within

1174 the region:

$$w = \frac{\epsilon_i + \epsilon_j - 2\epsilon_i\epsilon_j}{1 - \epsilon_i - \epsilon_j + 2\epsilon_i\epsilon_j}. \quad (6.4)$$

### 1175 **6.3.3 $t\bar{t}W$ background data-driven estimation**

1176 -  $t\bar{t}W$  represents a major source of irreducible background contamination in SM and BSM  
1177 analyses with  $t\bar{t}t\bar{t}$  final states.

1178 - Measured cross section for  $t\bar{t}W$  background has been consistently higher than predicted  
1179 values as seen in previous analyses ( $t\bar{t}H/t\bar{t}W$  multilepton [62, 63] and  $t\bar{t}t\bar{t}$  [64, 65] analyses)  
1180 due to mismodeling, especially at higher  $N_{\text{jets}}$   
1181 (show postfit  $t\bar{t}W$  VR distribution)

1182 - Previously, this was handled by assigning large ad-hoc systematic uncertainties to  $t\bar{t}W$   
1183 events with 7 or more jets. - A semi-data-driven method originally employed in the R-parity-  
1184 violating-supersymmetry search [66] was used to mitigate this problem. - This method was  
1185 shown to be effective in the SM  $t\bar{t}t\bar{t}$  observation analysis [65] by improving  $t\bar{t}W$  modeling  
1186 especially in the showering step and switching  $t\bar{t}W$  systematic uncertainties from predomi-  
1187 nantly modeling to statistical.

1188 - MC kinematic distributions for  $t\bar{t}W$  are applied with correction factors obtained from a  
1189 fitted function parameterized in  $N_{\text{jets}}$ .

1190 - The function describes scaling patterns for QCD [67] can be represented by ratio of suc-  
1191 cessive exclusive jet cross-sections

$$R_{(n+1)/n} = e^{-b} + \frac{\bar{n}}{n+1} = a_0 + \frac{a_1}{1 + (j-4)}, \quad (6.5)$$

1192 where  $n$  is the number of jets in addition to the hard process,  $j$  is the inclusive number of  
 1193 jets, and  $\bar{n}$  is the expectation value for the Poisson distribution for exclusive jet cross-section  
 1194 at jet multiplicity  $n$ , described as  $P_n = \sigma_n / \sigma_{\text{tot}}$ .

1195 - Same-sign di-lepton  $t\bar{t}W$  events dominate the  $t\bar{t}W$  background and produce 4 jets in the  
 1196 matrix element at tree level for the hard process, so  $n$  is defined starting from 5 jets and  $j$   
 1197 is defined as inclusive number of jets with 4 or more jets, or  $j \equiv n + 4$ .

1198 - The two terms in the equation correspond respectively to staircase and Poisson scaling  
 1199 between successive multiplicity cross sections, defined as constant ratios  $e^{-b}$  and ratios be-  
 1200 tween Poisson probability for  $n + 1$  and  $n$  jets. Staircase scaling is sensitive to events with  
 1201 high jet multiplicity, while Poisson scaling is sensitive to events with low jet multiplicity [67].

1202 - The scaling pattern can then be re-parameterized in  $a_0$  and  $a_1$  to obtain the  $t\bar{t}W$  yield at  
 1203  $j'$

$$\text{Yield}_{t\bar{t}W(j')} = \text{Yield}_{t\bar{t}W(j=4)} \times \prod_{j=4}^{j'-1} \left( a_0 + \frac{a_1}{1 + (j - 4)} \right) \quad (6.6)$$

1204 where  $j'$  is defined as  $j' \equiv j + 1$  with  $j \geq 4$  since the parameterization starts at the 4<sup>th</sup> jet.

1205 The  $t\bar{t}W$  yield at the 4-jet bin can be represented by a normalization factor applied to  $t\bar{t}W$   
 1206 MC simulation as  $\text{Yield}_{t\bar{t}W(j=4)} = \text{NF}_{t\bar{t}W(j=4)} \times \text{MC}_{j=4}$ .

1207 To account for the disparity in  $t\bar{t}W^+$  and  $t\bar{t}W^-$  cross-section, assuming the scaling is the  
 1208 same for both processes,  $\text{NF}_{t\bar{t}W(j=4)}$  can be further split into  $\text{NF}_{t\bar{t}W^+(j=4)}$  and  $\text{NF}_{t\bar{t}W^-(j=4)}$ .

1209 Both NFs are left free-floating to constrain  $t\bar{t}W$  yields at the 4-jet bin in CR 1b(+) and CR  
 1210 1b(-).

1211 The final  $N_{\text{jets}}$ -parameterized function can then be represented by  $\text{NF}_{t\bar{t}W(j')}$  as

$$\text{NF}_{t\bar{t}W(j')} = \left( \text{NF}_{t\bar{t}W^+(j=4)} + \text{NF}_{t\bar{t}W^-(j=4)} \right) \times \prod_{j=4}^{j'-1} \left( a_0 + \frac{a_1}{1 + (j - 4)} \right). \quad (6.7)$$

1212 This normalization is calculated and applied separately for each sub-sample of  $t\bar{t}W^+$  and  
1213  $t\bar{t}W^-$  in an  $N_{\text{jets}}$  bin for  $4 \leq N_{\text{jets}} < 10$ .

1214 Due to small contributions in the CRs, events with  $N_{\text{jets}} < 4$  and  $N_{\text{jets}} \geq 10$  are not  
1215 normalized with this scheme.

1216 Instead,  $N_{\text{jets}} < 4$   $t\bar{t}W$  events are fitted by propagating normalization in the 4-jet bin  
1217 without additional shape correction. The correction factor for  $t\bar{t}W$  events with  $N_{\text{jets}} \geq$   
1218 10 is obtained by summing up the overflow from  $N_{\text{jets}} = 10$  to  $N_{\text{jets}} = 12$ , described as  
1219  $\sum_{j'=10}^{12} \prod_{j=4}^{j'-1} \left( a_0 + \frac{a_1}{1+(j-4)} \right)$ . Events with  $N_{\text{jets}} \geq 13$  are negligible and thus not included  
1220 in the sum.

## 1221 Control region definitions

1222 Four control regions CR  $t\bar{t}W^+$ , CR  $t\bar{t}W^-$ , CR 1b(+), CR 1b(-) are constructed to fit  
1223  $\text{NF}_{t\bar{t}W^\pm(j=4)}$  and the scaling parameters  $a_0$ ,  $a_1$  for the  $t\bar{t}W$  background, as well as vali-  
1224 dating the parameterization.

1225 Events in CR  $t\bar{t}W^\pm$  are required to contain at least two  $b$ -tagged jets similar to the SR to  
1226 determine the  $t\bar{t}W$  normalization within an SR-related phase space. Orthogonality with SR  
1227 is satisfied by requiring  $H_{\text{T}} < 500$  GeV or  $N_{\text{jets}} < 6$  when  $N_b = 2$ , and  $H_{\text{T}} < 500$  GeV when  
1228  $N_b \geq 3$ .

1229 The remaining CR 1b( $\pm$ ) require events to have  $H_{\text{T}} > 500$  GeV and at least four jets to  
1230 encompass events with high  $N_{\text{jets}}$ , which can be used to determine the  $t\bar{t}W$  jet multiplic-

ity spectrum for fitting  $a_{0,1}$ . The selection criteria also include exactly one  $b$ -tagged jet to maintain orthogonality with SR. Assuming the  $t\bar{t}W$  jet multiplicity distribution is similar across different  $N_b$ , a fitted  $N_{\text{jets}}$  distribution in CR 1b( $\pm$ ) can be used to describe the  $t\bar{t}W$  parameterization at higher  $N_{\text{jets}}$ . The full selection criteria for all four regions are shown in ??

Validating the  $t\bar{t}W$  parameterization in Equation 6.7 makes use of the unique charge asymmetry in  $t\bar{t}W$  production that's not present in other background or signal processes. The number of events with all negatively charged leptons is subtracted from that of events with all positively charged leptons, which cancels out charge symmetric events and leaves the  $t\bar{t}W$  background. Validation is done via a statistical-only (stat-only) fit to the  $t\bar{t}W$  MC prediction in CR 1b( $\pm$ ).

# Chapter 7. Systematic Uncertainties

(nuisance parameters)

- Heavy pruning, 10% on shape and normalization pruning (to fit timeline?)

## 7.1 Experimental uncertainties

Instrumental & minor:

- uncertainty on the integrated luminosity of the 2015-2018 Run 2 data set is 0.83%, obtained by the LUCID-2 detector for the primary luminosity measurements complemented by the ID and calorimeters

- Pile-up modeling in MC was calibrated to data through pile-up reweighting, resulting in a set of calibration SFs and associated uncertainties.

In general, calibrating MC simulations to match performance in data incurs uncertainties associated with the MC-to-data scale factors obtained from the calibration, which are in turn propagated to observables in the analysis.

### 7.1.1 Leptons

The trigger/reconstruction/ID/isolation efficiencies of electrons and muons (with separate systematic and statistical components for muon) differ between MC simulation and data, and require correction in the form of SFs with its associated uncertainties.

Similarly, electron and muon energy-momentum scale and resolution also incur uncertainties from MC-to-data correction, calculated by varying scale and resolution during simulations.

Muons have additional uncertainties for charge-dependent and charge-independent momen-

tum scale, and detector-specific (ID, MS, CB) track resolution.

The charge identification/ECIDS efficiency also gives rise to an additional uncertainty component.

## 7.1.2 Jets

Experimental uncertainties on jets are dominated by flavor tagging-related uncertainties, with subleading contributions from jet energy scale/resolution (JES/JER) and NNJvt calibration.

### Jet energy scale

JES and its associated uncertainties are determined using data from test-beam and LHC collisions and MC simulated samples, decomposed into uncorrelated components:

- Effective nuisance parameters (NPs): 15  $p_T$ -dependent uncertainty components in total measured in situ, grouped based on their origin (2 detector-related, 4 modeling-related, 3 mixed, 6 statistical-related)
- $\eta$  intercalibration: 6 total components (1 modeling-related, 4 non-closure and 1 statistical-related) associated with the correction of the forward jets' ( $0.8 \leq |\eta| < 4.5$ ) energy scale to that of the central jets ( $|\eta| < 0.8$ ).
- Flavor composition/response: 2 components for relative quark-gluon flavor compositions in background and signal samples, and 2 components for uncertainty in responses to gluon-initiated versus quark-initiated jets

- Pile-up subtraction: 4 components, two for uncertainty in  $\mu$  (`OffsetMu`) and  $N_{\text{PV}}$  (`OffsetNPV`) modeling, one for residual  $p_{\text{T}}$ -dependency (`PtTerm`) and one for topology dependence on the per-event  $p_{\text{T}}$  density modeling (`RhoTopology`)
- Punch-through effect treatment: two terms (AF3 fast simulation and full detector simulations) for GSC punch-through jet response correction between data and MC.
- Non-closure: one term to account for difference between AF3-simulated samples and full detector simulations.
- High- $p_{\text{T}}$  single-particle response: one term for response to high- $p_{\text{T}}$  jets from single-particle and test-beam measurements
- $b$ -jets response: one term for uncertainty in the response to  $b$ -jets

## Jet energy resolution

JER measured separately in data and MC simulations using in situ techniques as a function of  $p_{\text{T}}$  and  $\eta$  for a given jet. Associated uncertainties are defined as quadratic difference between data and MC simulations.

This analysis uses the full JER uncertainty set provided for Run 2 searches with 14 total components: 12 effective NPs and 2 for difference between data and MC simulation, separately for AF3 and FS.

## Jet vertex tagging

JVT associated uncertainty is obtained by varying the JVT efficiency correction SFs within their range of uncertainty. This uncertainty accounts for remaining contamination from pile-up jets after applying pile-up suppression and MC generator choice.



## Flavor tagging

SFs for  $b$ -jets tagging efficiencies and  $c$ -/light-jets mis-tagging rates are obtained as a function of  $p_T$  for  $b$ -/ $c$ -/light-jets and PCB scores. The covariance matrix of systematic and statistical uncertainties is diagonalized and reduced in dimensions using principle component analysis (PCA), resulting in a set of orthogonal NPs: 85 for  $b$ -jets, 56 for  $c$ -jets and 42 for light-jets.

### 7.1.3 Missing transverse energy

Uncertainties for  $E_T^{\text{miss}}$  arise from possible miscalibration of its soft-track component, and are estimated using data-MC comparison of the  $p_T$  scale and resolution between the hard and soft  $E_T^{\text{miss}}$  terms. These uncertainties are represented by three independent terms: one for scale uncertainty and two resolution uncertainties for the parallel and perpendicular components.

## 7.2 Modeling uncertainties

### 7.2.1 Signal and irreducible background uncertainties

- scale variations - 6-point variation method, varying  $\mu_R$  &  $\mu_F$  vs central values to cover missing higher-order QCD corrections (signal & all major irreducible background)

$(\mu_R, \mu_F) = (0.5, 0.5), (0.5, 1), (1, 0.5), (1, 2), (2, 1), (2, 2)$  - pdf uncertainty: flat 1% for  $t\bar{t}Z'$ ,

$t\bar{t}t\bar{t}$ ,  $t\bar{t}Z$ ,  $t\bar{t}H$ , envelope of differences between nominal vs. other pdf choices for  $t\bar{t}t$

$t\bar{t}Z'$  signal

- parton distribution function: 1%

Table 7.1: Summary of the experimental systematic uncertainties considered in this analysis.

Systematic uncertainty	Terms	Scale [%]
<b>Event</b>		
Luminosity	1	0.83
Pile-up reweighting	1	$\mathcal{O}(1) \sim \mathcal{O}(10)$
<b>Electrons</b>		
Trigger efficiency	1	$\mathcal{O}(10^{-2}) \sim \mathcal{O}(10^{-1})$
Reconstruction efficiency <sup>†</sup>	1	$\mathcal{O}(10^{-1}) \sim \mathcal{O}(1)$
Identification efficiency <sup>†</sup>	1	$\mathcal{O}(10^{-1}) \sim \mathcal{O}(1)$
Isolation efficiency <sup>†</sup>	1	$\mathcal{O}(10^{-1}) \sim \mathcal{O}(1)$
Energy scale	1	$\mathcal{O}(10^{-2}) \sim \mathcal{O}(10^{-1})$
Energy resolution	1	$\mathcal{O}(10^{-2}) \sim \mathcal{O}(10^{-1})$
Charge identification (ECIDS) efficiency <sup>†</sup>	1	$\mathcal{O}(10^{-1}) \sim \mathcal{O}(1)$
<b>Muons</b>		
Trigger efficiency (stat/sys)	2	$\mathcal{O}(10^{-1}) \sim \mathcal{O}(1)$
Track-to-vertex association efficiency (stat/sys)	2	$\mathcal{O}(10^{-2}) \sim \mathcal{O}(10^{-1})$
Reconstruction/identification efficiency (stat/sys)	2	$\mathcal{O}(10^{-1}) \sim \mathcal{O}(1)$
Low- $p_T$ (< 15 GeV) reconstruction/identification efficiency (stat/sys)	2	$\mathcal{O}(10^{-1}) \sim \mathcal{O}(1)$
Isolation efficiency (stat/sys)	2	$\mathcal{O}(10^{-1}) \sim \mathcal{O}(1)$
Charge-independent momentum scale	1	$\mathcal{O}(10^{-2}) \sim \mathcal{O}(10^{-1})$
Charge-dependent momentum scale	4	$\mathcal{O}(10^{-2}) \sim \mathcal{O}(10^{-1})$
Energy resolution (CB)	1	$\mathcal{O}(10^{-2}) \sim \mathcal{O}(10^{-1})$
Energy resolution (ID & MS)*	2	$\mathcal{O}(10^{-2}) \sim \mathcal{O}(10^{-1})$
<b>Jets</b>		
JES effective NP	15	$\mathcal{O}(10^{-2}) \sim \mathcal{O}(1)$
JES $\eta$ intercalibration	3	$\mathcal{O}(10^{-1}) \sim \mathcal{O}(1)$
JES flavor composition	2	$\mathcal{O}(10^{-1}) \sim \mathcal{O}(1)$
JES flavor response	1	$\mathcal{O}(10^{-1}) \sim \mathcal{O}(1)$
JES pile-up	4	$\mathcal{O}(10^{-1}) \sim \mathcal{O}(10)$
JES punch-through (FS/AF3*)	2	$< \mathcal{O}(10^{-2})$
JES non-closure	1	$\mathcal{O}(10^{-2}) \sim \mathcal{O}(10^{-1})$
JES high- $p_T$ single particle	1	$< \mathcal{O}(10^{-2})$
JES $b$ -jet response	1	$\mathcal{O}(10^{-1}) \sim \mathcal{O}(1)$
JER effective NP	12	$\mathcal{O}(10^{-1}) \sim \mathcal{O}(1)$
JER data/MC (FS/AF3*)	2	$\mathcal{O}(10^{-1}) \sim \mathcal{O}(1)$
JVT efficiency	1	$\mathcal{O}(10^{-1}) \sim \mathcal{O}(1)$
GN2v01 $b$ -tagging efficiency ( $b$ -jets)	85	$\mathcal{O}(10^{-2}) \sim \mathcal{O}(1)$
GN2v01 $b$ -tagging efficiency ( $c$ -jets)	56	$\mathcal{O}(10^{-2}) \sim \mathcal{O}(1)$
GN2v01 $b$ -tagging efficiency (light-jets)	42	$\mathcal{O}(10^{-2}) \sim \mathcal{O}(1)$
<b><math>E_T^{\text{miss}}</math>-Terms</b>		
Track-based soft term for transversal resolution	1	$\mathcal{O}(10^{-2}) \sim \mathcal{O}(10^{-1})$
Track-based soft term for longitudinal resolution	1	$\mathcal{O}(10^{-2}) \sim \mathcal{O}(10^{-1})$
Track-based soft term for longitudinal scale	1	$\mathcal{O}(10^{-2}) \sim \mathcal{O}(10^{-1})$

1324 **SM  $t\bar{t}t\bar{t}$  background**

- 1325 - cross section: 20% from NLO prediction in QCD+EW
- 1326 - generator uncertainty: madgraph5\_amc@nlo (nominal) vs sherpa 2.2.10
- 1327 - parton shower uncertainty: pythia8 (nominal) vs herwig7

1328 **SM  $t\bar{t}t$  background**

- 1329 - cross section: 30% from NLO prediction in QCD+EW
- 1330 - additional  $b$ -jets: 50% for  $t\bar{t}t$  events with 4+ truth  $b$ -jets

1331  **$t\bar{t}W$ ,  $t\bar{t}Z$ ,  $t\bar{t}H$  background**

- 1332 - cross section:  $t\bar{t}Z$  12%,  $t\bar{t}H$  10% (from CERN yellow report)
- 1333 no cross-section and pdf uncertainties for  $t\bar{t}W$  since normalizations and jet multiplicity spec-
- 1334 trum are estimated with data-driven method
- 1335 - parton shower uncertainty:  $t\bar{t}H$  powhegbox+pythia8 (nominal) vs powhegbox+herwig7
- 1336 - additional  $b$ -jets: events with additional HF jets can contaminate SR and are challenging
- 1337 to model w/ MC - 50% for events with an additional truth  $b$ -jet not from top-quark decay,
- 1338 additional 50% for 2 or more
- 1339 - generator uncertainty **table?**
- 1340 •  $t\bar{t}W$ - sherpa (nominal) vs madgraph5\_amc@nlo
- 1341 •  $t\bar{t}Z$ - madgraph5\_amc@nlo (nominal) vs sherpa 2.2.10
- 1342 •  $t\bar{t}H$ - powheg8/PhPy8 (nominal) vs powheg8/PhPy8 pthard

## Other backgrounds

- $t(\bar{t})X$ : cross section 30%
- $VV$ : cross section (STDM-2018-03) uncorrelated 20%/50%/60% for events with 3-4/5+ jets; events with 1+ truth  $b$ -jets not from top decay 50%
- $t\bar{t}VV, VVV, VH$ : cross section 50%; additional  $b$ -jets same as  $VV$

## 7.2.2 Reducible background uncertainties

- Electron charge misidentification background:
- Material and internal (low  $\gamma^*$ ) conversion background: estimated based on data/MC differences in a region enriched with  $Z \rightarrow \ell^+ \ell^- \gamma$ ; 30% & 21% for material & internal conversion
- Heavy-flavor non-prompt lepton background: estimated based on data/MC differences in CR/SR distributions, ranging from 20-100%
- Light-flavor decays and other fake/non-prompt background: Conservative normalization uncertainty of 100% for light-flavor non-prompt lepton background (ATLAS-CONF-2019-045), 30% for normalization of all other fake backgrounds.
- +HF: contaminates SR phase space with large  $b$ -jet multiplicity, estimated from data/MC discrepancy, 30% for events with

Table 7.2: Caption

Systematic uncertainty	Terms	Scale [%]
<b><math>t\bar{t}Z'</math> modeling</b>		
Renormalization & factorization scale		
PDF		
<b>SM <math>t\bar{t}t\bar{t}</math> modeling</b>		
Cross-section		
Renormalization & factorization scale		
PDF		
Generator choice		
Parton shower model		
<b>SM <math>t\bar{t}t</math> modeling</b>		
Cross-section		
Renormalization & factorization scale		
PDF		
Additional $b$ -jets		
<b><math>t\bar{t}W</math> modeling</b>		
Renormalization & factorization scale		
Generator choice		
Additional $b$ -jets		
<b><math>t\bar{t}Z</math> modeling</b>		
Cross-section		
Renormalization & factorization scale		
PDF		
Generator choice		
Additional $b$ -jets		
<b><math>t\bar{t}H</math> modeling</b>		
Cross-section		
Renormalization & factorization scale		
PDF		
Generator choice		
Parton shower model		
Additional $b$ -jets		
<b>Other background modeling</b>		
Cross-section		
Additional $b$ -jets		

Table 7.3: Caption

Systematic uncertainty	Terms	Scale [%]
<b>Reducible SM background</b>		
$t\bar{t}/V/t+\text{jets}$	2	
Charge misidentification	1	
<b>Fake &amp; non-prompt background</b>		
Low $\gamma^*$	1	
Material conversion	1	
HF $e$	1	
HF $\mu$	1	
Light-flavor decays	1	100
Other fakes	1	30

# Chapter 8. Results

## 8.1 Statistical analysis

This section provides an overview of the statistical methods needed to interpret the collected and simulated data to estimate unknown physics parameters and determine compatibility between data and the analysis hypothesis. For the BSM resonance search, the null hypothesis  $H_0$  assumes only SM background contributions and none from any new resonance in the data.

### 8.1.1 Profile likelihood fit

Given a set of observed data points  $\mathbf{x} = [x_1, x_2, \dots]$  and unknown parameters  $\boldsymbol{\theta} = [\theta_1, \theta_2, \dots, \theta_n]$ , the maximum likelihood method aims to find an estimate  $\hat{\boldsymbol{\theta}}$  that maximizes the joint probability function  $f(\mathbf{x}, \boldsymbol{\theta})$ , or in other words the set of parameters that gives the highest probability of observing the collected data points for a particular model. The function to be maximized for this purpose is the log-likelihood (LLH) function  $\ln \mathcal{L}(\mathbf{x}, \boldsymbol{\theta})$  where  $\mathcal{L}(\mathbf{x}, \boldsymbol{\theta}) \equiv \prod_i f(x_i, \boldsymbol{\theta})$  is defined as the likelihood (LH) function. The LLH is maximized when  $\partial/\partial\theta_i (\ln \mathcal{L}) = 0$  for each parameter  $\theta_i$ .

For an usual binned physics analysis, the above variables for the LH function  $\mathcal{L}$  can be expressed as nuisance parameters (NP)  $\boldsymbol{\theta}$  and number of events for a model  $N_i(\mu)$  for the  $i^{\text{th}}$  bin, where  $\mu$  is the targeted parameter of interest (POI). In this analysis,  $N_i$  is assumed to follow a Poisson distribution and depends on the following quantities: the signal strength  $\mu$  defined as the ratio of observed to expected cross sections  $\sigma_{\text{obs}}/\sigma_{\text{exp}}$ ; nuisance parameters  $\boldsymbol{\theta}$  which represents the effects of systematic uncertainties, implemented in the LH function as Gaussian constraints; and normalization factors (NFs)  $\boldsymbol{\lambda}$  that control the

1381 normalization of background components that do not have a well-known cross section. The  
 1382 Poisson probability of observing exactly  $N_i$  events for an expected number of event  $n_i$  is

$$\mathcal{P}(N_i|n_i(\mu, \boldsymbol{\lambda})) = \frac{n_i^{N_i} e^{-n_i}}{N_i!}. \quad (8.1)$$

1383 The expected Poisson event number in a bin  $i$  can be parameterized as

$$n_i = \mu s_i(\boldsymbol{\theta}) + \sum_j \lambda_j b_{ij}(\boldsymbol{\theta}), \quad (8.2)$$

1384 where  $s_i$  is the number of signal events in bin  $i$  of every region, and  $b_{ij}$  is the number of  
 1385 events for a certain background source index  $j$  in bin  $i$ . The LH function in this analysis  
 1386 can be written as

$$\mathcal{L}(\mathbf{N}|\mu, \boldsymbol{\theta}, \boldsymbol{\lambda}) = \left( \prod_i \mathcal{P}(N_i|n_i) \right) \cdot \prod_k \mathcal{G}(\theta_k), \quad (8.3)$$

1387 where  $\mathcal{G}(\theta_k)$  is the Gaussian constraint for a NP  $k$ . The signal significance  $\mu$  and NFs  $\boldsymbol{\lambda}$  are  
 1388 left unconstrained and are fitted simultaneously in the profile LH fit. From Neyman-Person  
 1389 lemma [citation](#), the optimal test statistic for hypothesis testing is a function dependent on  
 1390 the profile LH ratio defined as

$$q_\mu \equiv -2 \ln \frac{\mathcal{L}(\mu, \hat{\boldsymbol{\theta}}_\mu, \hat{\boldsymbol{\lambda}}_\mu)}{\mathcal{L}(\hat{\mu}, \hat{\boldsymbol{\theta}}, \hat{\boldsymbol{\lambda}})}, \quad (8.4)$$

1391 where  $\hat{\mu}$ ,  $\hat{\boldsymbol{\theta}}$  and  $\hat{\boldsymbol{\lambda}}$  are parameter values that optimally maximizes the LH function, and  $\hat{\boldsymbol{\theta}}_\mu$ ,  
 1392  $\hat{\boldsymbol{\lambda}}_\mu$  are NP and NF values respectively that maximize the LH function for a given  $\mu$ .



### 8.1.2 Exclusion limits

## 8.2 Fit results

### Fit setup

- Plain Asimov fit (**only mentioning briefly**): all regions included; simulated data used in the fit match exactly to MC prediction with nominal  $\mu_{t\bar{t}Z'}$  set to 0 and allowed to free-float.

Purpose: to perform studies on optimizing fitted parameters and expected sensitivity; refining background estimation techniques; optimizing region definition and object definition

- Real SRs-blinded fit: similar to plain Asimov, but use observed data in CRs.

Purpose: study the behavior of background estimation using real observed data in CRs on Asimov data in SRs and assessing the influence of statistical effects on fitted parameters and expected sensitivity

- Real SRs-unblinded/ $H_T$  fit: all regions included,

### Limits

1408 **Chapter 9. Summary**

# References

- [1] ATLAS Collaboration. *The ATLAS Experiment at the CERN Large Hadron Collider*. JINST 3 (2008), S08003 (cit. on p. 2).
- [2] C. Burgard and D. Galbraith. *Standard Model of Physics*. URL: <https://texample.net/model-physics/> (visited on 06/02/2025) (cit. on p. 4).
- [3] CMS Collaboration. *Search for  $t\bar{t}H$  production in the  $H \rightarrow b\bar{b}$  decay channel with leptonic  $t\bar{t}$  decays in proton–proton collisions at  $\sqrt{s} = 13$  TeV*. JHEP 03 (2019), p. 026. arXiv: 1804.03682 [hep-ex] (cit. on p. 7).
- [4] A. Pich. *The Standard Model of electroweak interactions. 2004 European School of High-Energy Physics*. Feb. 2005, pp. 1–48. arXiv: hep-ph/0502010 [hep-ex] (cit. on p. 13).
- [5] P. Higgs. *Broken symmetries and the masses of gauge bosons*. Phys. Rev. Lett. 13 (16 1964), pp. 508–509 (cit. on p. 13).
- [6] P. Higgs. *Broken symmetries, massless particles and gauge fields*. Physics Letters 12.2 (1964), pp. 132–133. ISSN: 0031-9163 (cit. on p. 13).
- [7] F. Englert and R. Brout. *Broken Symmetry and the Mass of Gauge Vector Mesons*. Phys. Rev. Lett. 13 (9 1964), pp. 321–323 (cit. on p. 13).

- [8] ATLAS Collaboration. *Observation of a new particle in the search for the Standard Model Higgs boson with the ATLAS detector at the LHC*. *Phys. Lett. B* 716 (2012), p. 1. arXiv: 1207.7214 [hep-ex] (cit. on p. 14).
- [9] CMS Collaboration. *Observation of a new boson at a mass of 125 GeV with the CMS experiment at the LHC*. *Phys. Lett. B* 716 (2012), p. 30. arXiv: 1207.7235 [hep-ex] (cit. on p. 14).
- [10] J. Ellis. *Higgs Physics. 2013 European School of High-Energy Physics*. 2015, pp. 117–168. arXiv: 1312.5672 [hep-ph] (cit. on pp. 15, 16).
- [11] P. Langacker. *The Physics of Heavy  $Z'$  Gauge Bosons*. *Rev. Mod. Phys.* 81 (2009), pp. 1199–1228. arXiv: 0801.1345 [hep-ph] (cit. on pp. 16, 17).
- [12] G. Ferretti and D. Karateev. *Fermionic UV completions of composite Higgs models*. *Journal of High Energy Physics* 2014.3 (Mar. 2014). ISSN: 1029-8479 (cit. on p. 17).
- [13] L. Vecchi. *A dangerous irrelevant UV-completion of the composite Higgs*. *JHEP* 02 (2017), p. 094. arXiv: 1506.00623 [hep-ph] (cit. on p. 17).
- [14] K. Agashe, A. Delgado, M. J. May, and R. Sundrum.  *$RS1$ , custodial isospin and precision tests*. *JHEP* 08 (2003), p. 050. arXiv: hep-ph/0308036 [hep-ph] (cit. on p. 17).
- [15] K. Agashe, R. Contino, and A. Pomarol. *The Minimal composite Higgs model*. *Nucl. Phys. B* 719 (2005), pp. 165–187. arXiv: hep-ph/0412089 [hep-ph] (cit. on p. 17).
- [16] N. Greiner, K. Kong, J.-C. Park, S. C. Park, and J.-C. Winter. *Model-independent production of a top-philic resonance at the LHC*. *Journal of High Energy Physics* 2015.4 (2015), p. 29. ISSN: 1029-8479 (cit. on pp. 17–19).

- [17] J. H. Kim, K. Kong, S. J. Lee, and G. Mohlabeng. *Probing TeV scale top-philic resonances with boosted top-tagging at the high luminosity LHC*. *Phys. Rev. D* 94 (3 2016), p. 035023 (cit. on p. 17).
- [18] ATLAS Collaboration. *Standard Model Summary Plots October 2023*. ATL-PHYS-PUB-2023-039. 2023. URL: <https://cds.cern.ch/record/2882448> (cit. on p. 23).
- [19] ATLAS Collaboration. *Electron reconstruction and identification in the ATLAS experiment using the 2015 and 2016 LHC proton–proton collision data at  $\sqrt{s} = 13$  TeV*. *Eur. Phys. J. C* 79 (2019), p. 639. arXiv: 1902.04655 [physics.ins-det] (cit. on pp. 26, 41–43).
- [20] ATLAS Collaboration. *Performance of the ATLAS track reconstruction algorithms in dense environments in LHC Run 2*. *Eur. Phys. J. C* 77 (2017), p. 673. arXiv: 1704.07983 [hep-ex] (cit. on p. 31).
- [21] T. Cornelissen et al. *Concepts, design and implementation of the ATLAS New Tracking (NEWT)*. Tech. rep. Geneva: CERN, 2007. URL: <https://cds.cern.ch/record/1020106> (cit. on p. 31).
- [22] A. Salzburger and on behalf of the ATLAS Collaboration. *Optimisation of the ATLAS Track Reconstruction Software for Run-2*. *Journal of Physics: Conference Series* 664.7 (2015), p. 072042 (cit. on p. 31).
- [23] R. Frühwirth. *Application of Kalman filtering to track and vertex fitting*. *Nucl. Instrum. Methods Phys. Res. A* 262.2 (1987), pp. 444–450. ISSN: 0168-9002 (cit. on p. 31).
- [24] T. Cornelissen et al. *The global  $\chi^2$  track fitter in ATLAS*. *Journal of Physics: Conference Series* 119.3 (2008), p. 032013 (cit. on p. 31).

- [25] ATLAS Collaboration. *Improved electron reconstruction in ATLAS using the Gaussian Sum Filter-based model for bremsstrahlung*. ATLAS-CONF-2012-047. 2012. URL: <https://cds.cern.ch/record/1449796> (cit. on p. 31).
- [26] D. Wicke. *A new algorithm for solving tracking ambiguities*. Tech. rep. Oct. 1998. URL: <https://cds.cern.ch/record/2625731> (cit. on p. 32).
- [27] ATLAS Collaboration. *Reconstruction of primary vertices at the ATLAS experiment in Run 1 proton–proton collisions at the LHC*. *Eur. Phys. J. C* **77** (2017), p. 332. arXiv: 1611.10235 [[physics.ins-det](#)] (cit. on p. 32).
- [28] W. Waltenberger, R. Frühwirth, and P. Vanlaer. *Adaptive vertex fitting*. *Journal of Physics G: Nuclear and Particle Physics* **34.12** (2007), N343 (cit. on p. 32).
- [29] ATLAS Collaboration. *Secondary vertex finding for jet flavour identification with the ATLAS detector*. ATL-PHYS-PUB-2017-011. 2017. URL: <https://cds.cern.ch/record/2270366> (cit. on p. 32).
- [30] ATLAS Collaboration. *Topological cell clustering in the ATLAS calorimeters and its performance in LHC Run 1*. *Eur. Phys. J. C* **77** (2017), p. 490. arXiv: 1603.02934 [[hep-ex](#)] (cit. on pp. 33, 34).
- [31] ATLAS Collaboration. *Jet reconstruction and performance using particle flow with the ATLAS Detector*. *Eur. Phys. J. C* **77** (2017), p. 466. arXiv: 1703.10485 [[hep-ex](#)] (cit. on p. 35).
- [32] M. Cacciari, G. P. Salam, and G. Soyez. *The anti-kt jet clustering algorithm*. *Journal of High Energy Physics* **2008.04** (2008), p. 063 (cit. on p. 35).

- [33] ATLAS Collaboration. *Jet energy scale and resolution measured in proton–proton collisions at  $\sqrt{s} = 13$  TeV with the ATLAS detector*. *Eur. Phys. J. C* **81** (2021), p. 689. arXiv: [2007.02645 \[hep-ex\]](#) (cit. on p. 36).
- [34] ATLAS Collaboration. *Jet energy scale measurements and their systematic uncertainties in proton–proton collisions at  $\sqrt{s} = 13$  TeV with the ATLAS detector*. *Phys. Rev. D* **96** (2017), p. 072002. arXiv: [1703.09665 \[hep-ex\]](#) (cit. on p. 36).
- [35] ATLAS Collaboration. *Transforming jet flavour tagging at ATLAS*. Tech. rep. Submitted to: Nature Communications. Geneva: CERN, 2025. arXiv: [2505.19689](#) (cit. on pp. 37–39).
- [36] A. Vaswani et al. *Attention Is All You Need*. 2023. arXiv: [1706.03762 \[cs.CL\]](#) (cit. on p. 37).
- [37] ATLAS Collaboration. *Measurements of  $b$ -jet tagging efficiency with the ATLAS detector using  $t\bar{t}$  events at  $\sqrt{s} = 13$  TeV*. *JHEP* **08** (2018), p. 089. arXiv: [1805.01845 \[hep-ex\]](#) (cit. on p. 40).
- [38] ATLAS Collaboration. *Electron and photon performance measurements with the ATLAS detector using the 2015–2017 LHC proton–proton collision data*. *JINST* **14** (2019), P12006. arXiv: [1908.00005 \[hep-ex\]](#).
- [39] ATLAS Collaboration. *Electron Identification with a Convolutional Neural Network in the ATLAS Experiment*. ATL-PHYS-PUB-2023-001. 2023. URL: <https://cds.cern.ch/record/2850666> (cit. on p. 43).
- [40] ATLAS Collaboration. *Muon reconstruction and identification efficiency in ATLAS using the full Run 2 pp collision data set at  $\sqrt{s} = 13$  TeV*. *Eur. Phys. J. C* **81** (2021), p. 578. arXiv: [2012.00578 \[hep-ex\]](#) (cit. on pp. 43–45).

- [41] ATLAS Collaboration. *Muon reconstruction performance of the ATLAS detector in proton–proton collision data at  $\sqrt{s} = 13$  TeV*. *Eur. Phys. J. C* **76** (2016), p. 292. arXiv: 1603.05598 [hep-ex] (cit. on p. 44).
- [42] ATLAS Collaboration. *Performance of missing transverse momentum reconstruction with the ATLAS detector using proton–proton collisions at  $\sqrt{s} = 13$  TeV*. *Eur. Phys. J. C* **78** (2018), p. 903. arXiv: 1802.08168 [hep-ex] (cit. on p. 45).
- [43] ATLAS Collaboration.  *$E_T^{miss}$  performance in the ATLAS detector using 2015–2016 LHC  $pp$  collisions*. ATLAS-CONF-2018-023. 2018. URL: <https://cds.cern.ch/record/2625233> (cit. on p. 46).
- [44] ATLAS Collaboration. *Observation of electroweak production of two jets in association with an isolated photon and missing transverse momentum, and search for a Higgs boson decaying into invisible particles at 13 TeV with the ATLAS detector*. *Eur. Phys. J. C* **82** (2022), p. 105. arXiv: 2109.00925 [hep-ex].
- [45] J. Alwall et al. *The automated computation of tree-level and next-to-leading order differential cross sections, and their matching to parton shower simulations*. *JHEP* **07** (2014), p. 079. arXiv: 1405.0301 [hep-ph] (cit. on pp. 49, 51, 52).
- [46] NNPDF Collaboration, R. D. Ball, et al. *Parton distributions for the LHC run II*. *JHEP* **04** (2015), p. 040. arXiv: 1410.8849 [hep-ph] (cit. on pp. 49, 51, 52).
- [47] T. Sjöstrand et al. *An introduction to PYTHIA 8.2*. *Comput. Phys. Commun.* **191** (2015), p. 159. arXiv: 1410.3012 [hep-ph] (cit. on pp. 49, 51, 52).
- [48] ATLAS Collaboration. *ATLAS Pythia 8 tunes to 7 TeV data*. ATL-PHYS-PUB-2014-021. 2014. URL: <https://cds.cern.ch/record/1966419> (cit. on pp. 51, 52).



- [49] S. Frixione, E. Laenen, P. Motylinski, and B. R. Webber. *Angular correlations of lepton pairs from vector boson and top quark decays in Monte Carlo simulations*. [JHEP 04 \(2007\), p. 081](#). arXiv: [hep-ph/0702198](#) (cit. on p. 51).
- [50] P. Artoisenet, R. Frederix, O. Mattelaer, and R. Rietkerk. *Automatic spin-entangled decays of heavy resonances in Monte Carlo simulations*. [JHEP 03 \(2013\), p. 015](#). arXiv: [1212.3460 \[hep-ph\]](#) (cit. on p. 51).
- [51] D. J. Lange. *The EvtGen particle decay simulation package*. [Nucl. Instrum. Meth. A 462 \(2001\), p. 152](#) (cit. on p. 51).
- [52] R. Frederix, D. Pagani, and M. Zaro. *Large NLO corrections in  $t\bar{t}W^\pm$  and  $t\bar{t}t\bar{t}$  hadroproduction from supposedly subleading EW contributions*. [JHEP 02 \(2018\), p. 031](#). arXiv: [1711.02116 \[hep-ph\]](#) (cit. on p. 51).
- [53] E. Bothmann et al. *Event generation with Sherpa 2.2*. [SciPost Phys. 7.3 \(2019\), p. 034](#). arXiv: [1905.09127 \[hep-ph\]](#) (cit. on pp. 51, 52).
- [54] S. Schumann and F. Krauss. *A parton shower algorithm based on Catani–Seymour dipole factorisation*. [JHEP 03 \(2008\), p. 038](#). arXiv: [0709.1027 \[hep-ph\]](#) (cit. on p. 51).
- [55] S. Höche, F. Krauss, M. Schönherr, and F. Siegert. *A critical appraisal of NLO+PS matching methods*. [JHEP 09 \(2012\), p. 049](#). arXiv: [1111.1220 \[hep-ph\]](#) (cit. on p. 51).
- [56] S. Höche, F. Krauss, M. Schönherr, and F. Siegert. *QCD matrix elements + parton showers. The NLO case*. [JHEP 04 \(2013\), p. 027](#). arXiv: [1207.5030 \[hep-ph\]](#) (cit. on p. 51).
- [57] S. Catani, F. Krauss, B. R. Webber, and R. Kuhn. *QCD Matrix Elements + Parton Showers*. [JHEP 11 \(2001\), p. 063](#). arXiv: [hep-ph/0109231](#) (cit. on p. 51).

- [58] S. Höche, F. Krauss, S. Schumann, and F. Siegert. *QCD matrix elements and truncated showers*. *JHEP* 05 (2009), p. 053. arXiv: 0903.1219 [hep-ph] (cit. on p. 51).
- [59] F. Cascioli, P. Maierhöfer, and S. Pozzorini. *Scattering Amplitudes with Open Loops*. *Phys. Rev. Lett.* 108 (2012), p. 111601. arXiv: 1111.5206 [hep-ph] (cit. on p. 51).
- [60] A. Denner, S. Dittmaier, and L. Hofer. *COLLIER: A fortran-based complex one-loop library in extended regularizations*. *Comput. Phys. Commun.* 212 (2017), pp. 220–238. arXiv: 1604.06792 [hep-ph] (cit. on p. 51).
- [61] F. Buccioni et al. *OpenLoops 2*. *Eur. Phys. J. C* 79.10 (2019), p. 866. arXiv: 1907.13071 [hep-ph] (cit. on p. 51).
- [62] ATLAS Collaboration. *Analysis of  $t\bar{t}H$  and  $t\bar{t}W$  production in multilepton final states with the ATLAS detector*. ATLAS-CONF-2019-045. 2019. URL: <https://cds.cern.ch/record/2693930> (cit. on p. 63).
- [63] ATLAS Collaboration. *Measurement of the total and differential cross-sections of  $t\bar{t}W$  production in  $pp$  collisions at  $\sqrt{s} = 13$  TeV with the ATLAS detector*. *JHEP* 05 (2024), p. 131. arXiv: 2401.05299 [hep-ex] (cit. on p. 63).
- [64] ATLAS Collaboration. *Evidence for  $t\bar{t}t\bar{t}$  production in the multilepton final state in proton–proton collisions at  $\sqrt{s} = 13$  TeV with the ATLAS detector*. *Eur. Phys. J. C* 80 (2020), p. 1085. arXiv: 2007.14858 [hep-ex] (cit. on p. 63).
- [65] ATLAS Collaboration. *Observation of four-top-quark production in the multilepton final state with the ATLAS detector*. *Eur. Phys. J. C* 83 (2023), p. 496. arXiv: 2303.15061 [hep-ex] (cit. on p. 63).

- 1580 [66] ATLAS Collaboration. *Search for  $R$ -parity-violating supersymmetry in a final state*  
1581 *containing leptons and many jets with the ATLAS experiment using  $\sqrt{s} = 13 \text{ TeV}$*   
1582 *proton–proton collision data.* [Eur. Phys. J. C 81 \(2021\), p. 1023](#). arXiv: [2106.09609](#)  
1583 [\[hep-ex\]](#) (cit. on p. 63).
- 1584 [67] E. Gerwick, T. Plehn, S. Schumann, and P. Schichtel. *Scaling Patterns for QCD Jets.*  
1585 [JHEP 10 \(2012\), p. 162](#). arXiv: [1208.3676](#) [\[hep-ph\]](#) (cit. on pp. 63, 64).